

Unified Algorithm for Aerosol Characterization Using Broad Spectrum Measurements from PACE's Ocean Color Instrument

Lorraine A. Remer¹, Omar Torres², Robert C. Levy², N. Christina Hsu²
Shana Mattoo^{3,2}, Hiren Jethva^{4,2}, Woogyung Vincent Kim^{5,2},
Yingxi Rona Shi^{1,2}, Vinay Kayetha^{6,2} and Jaehwa Lee^{5,2}

¹ Goddard Earth Science Technology and Research II, University of Maryland Baltimore County

²Earth Sciences Directorate, NASA Goddard Space Flight Center

³Science Systems and Applications Inc.

⁴Goddard Earth Science Technology and Research II, Morgan State University

⁵Earth Systems Science Interdisciplinary Center (ESSIC), University of Maryland College Park

⁶ Science and Technology Corporation, Hampton, 23666, USA

Corresponding author: Lorraine A. Remer (rem@umbc.edu)

Key Points:

- PACE OCI measures radiance across a broad spectrum allowing quantitative retrievals of aerosol loading, absorption and height
- Initial matchups with AERONET confirm retrieval of AOD within expectations of heritage algorithms
- Preliminary analysis suggests that single scattering albedo at 0.44 μm is retrieved to within ± 0.04

Version: 1.1

Release Date: Mar 2 2026

DOI: TBD

Table of Contents

	Abstract	3
	Plain Language Summary	3
	Keywords	4
	Version Description	4
1	Introduction	5
2	Context/Background	5
3	Algorithm Description	8
3.1	Scientific theory	8
3.2	Heritage Dark Target algorithm	10
3.3	Heritage Deep Blue algorithm	12
3.4	Heritage Near UV algorithm	13
3.5	Merging the three heritage algorithms	16
3.6	Algorithm input and output variables	19
3.7	UAA creative innovations	22
3.7.1	Adapting DT and DB heritage to OCI sensor characteristics	22
3.7.2	Extending DT for a SSA retrieval over ocean	24
3.7.3	DT/DB merge over land	27
3.7.4	Extrapolation of AOD to the UV over land	30
3.7.5	UAA NUV retrieval	35
3.7.6	AOD above clouds	37
3.7.7	Oxygen-B band retrievals of aerosol layer height	39
4	Algorithm Usage Constraints	42
5	Performance Assessment	43
5.1	Demonstration	43
5.2	Validation methods	49
5.3	Uncertainties	49
5.4	Validation errors	50
6	Algorithm Implementation	55
6.1	Algorithm availability	55
6.2	Input data access	55
6.3	Output data access	55
7	Significance Discussion	56
8	Open Research	57
9	Acknowledgements	57
	Contact Details	58
	References	60

Abstract

The launch of NASA's Plankton, Aerosols, Clouds, ocean Ecosystem (PACE) mission in 2024 with the Ocean Color Instrument (OCI) on board created new opportunity for characterizing aerosol properties from space. OCI observes Earth and its atmosphere across a broad spectral range from the ultraviolet (UV) to the shortwave infrared (SWIR). Heritage aerosol retrieval algorithms developed to for radiometers measuring in the visible to SWIR wavelengths such as the MODerate resolution Imaging Spectroradiometer (MODIS) have been successful in characterizing mid-visible aerosol optical depth (AOD) and indications of aerosol particle size but are less sensitive to aerosol particle absorption or aerosol layer height. Other heritage sensors measuring in the UV part of the spectrum such as the Total Ozone Mapping Spectrometer (TOMS) or the Ozone Monitoring Instrument (OMI) are sensitive to absorption and layer height but have insufficient information to constrain AOD in an aerosol retrieval. With OCI encompassing the entire spectral range of interest the Dark Target and Deep Blue algorithms from the MODIS tradition and Near UV algorithm from the TOMS/OMI tradition are brought together, adapted for OCI and unified for retrievals of AOD, particle size parameter, aerosol absorption and aerosol layer height. Adaptations include adjustment for OCI sensor characteristics, modification of cloud and snow masking routines, production of the traditional UV Aerosol Index at unprecedented 1.2 km resolution, merging of the Dark Target and Deep Blue retrievals over land, extrapolation of spectral AOD retrieved in the visible range into the UV range, use of Oxygen B bands for aerosol layer height, and retrieval of UV AOD above clouds that provides visualization of all-sky aerosol loading. Six months of retrievals have been compared with collocated AERONET AOD and single scattering albedo (SSA) to perform a preliminary validation. AOD is biased high for shorter wavelengths, especially over ocean, leading to asymmetrical error bounds for AOD. No similar bias is seen in the SSA retrievals which are exhibiting error bounds of ± 0.04 , at this stage. The results of the OCI Unified Aerosol Algorithm are quantitative characterization of the global aerosol system over ocean, vegetated and barren surfaces, in clear skies and above clouds.

Plain Language Summary

In this document we show how information about atmospheric aerosols (smoke, dust, particulate pollution) is obtained from measurements made by the Ocean Color Instrument (OCI) aboard

NASA's Plankton, Aerosols, Clouds, ocean Ecosystem (PACE) mission. OCI is the first NASA instrument that can measure radiance scattered back from the Earth-atmosphere system in a wide spectral range from the ultraviolet to the shortwave infrared. This broad spectrum allows us, for the first time, to unify three complementary aerosol algorithms to make use of OCI's broad information content. The result is a range of aerosol products produced with confidence that include a measure of how much aerosol there is in a scene (aerosol optical depth), how dark that aerosol is (aerosol absorption) and whether that aerosol is at ground level or higher up in the atmosphere. We apply the new unified algorithm to the first six months of OCI measurements so that we can determine whether the algorithm is working. It does work, and we can quantify how well it is working.

Keywords: aerosol, NASA PACE, Ocean Color Instrument, aerosol optical depth, aerosol single scattering albedo, aerosol layer height

Version Description

This is Version 1.1 of the Unified Aerosol Algorithm (UAA) ATBD. It is a lightly edited version, by Andrew Sayer, of the original submission (1.0) by PI Lorraine Remer (on Feb 24 2026).

1 Introduction

This Algorithm Theoretical Basis Document (ATBD) describes the Unified Aerosol Algorithm (UAA) that has been under development as part of the PACE Science and Applications Team and now runs in the PACE Science Data Segment operational processing environment. The ATBD describes the historical background to creating this algorithm and the key properties of the PACE Ocean Color Instrument (OCI) that allow for innovation and expansion of heritage algorithms. The document briefly introduces the three heritage algorithms that form the basis of the UAA and directs readers to previously published literature, as well as explains the innovations that allow the combination of the three heritage algorithms and push those algorithms beyond historical precedent. Algorithm inputs, outputs and ancillary data are listed and example output scenes illustrated. The ATBD presents preliminary uncertainty estimates on parameters using 6 months of retrievals, gives caveats for use and suggestions directions for future investigations. Much of the content in this ATBD is taken directly from a manuscript to be submitted for publication in the journal Atmospheric Measurement Techniques.

2 Context/Background

To determine aerosol loading and constrain some aerosol characteristics globally, we turn to satellite aerosol remote sensing. For decades satellite sensors have been observing the Earth system in specific wavelength bands covering the part of the reflected solar and emitted terrestrial wavelength ranges (Torres and Remer, 2013). Algorithms applied to these measurements have created many well-used data sets of quantitative aerosol characterization (Remer et al., 2020). The most pervasive of these products is aerosol optical depth (AOD) as a function of wavelength (i.e., spectral). AOD is a measure of aerosol loading in an optical sense and knowing aerosol loading is the fundamental parameter leading to estimates of aerosol effects in the energy budget, to identifying associations between aerosol amount and cloud properties, and to provide warning to populations when an air quality alert is forecasted. However, AOD by itself is only the first order parameter of interest. Other aerosol properties such as size, shape, absorption and layer height are necessary to reduce uncertainties in calculating aerosol effects on

energy balance, interaction with clouds, health, etc. (Szopa et al., 2021). Satellite aerosol remote sensing has had less success in achieving these other parameters.

The first aerosol remote sensing algorithms made use of satellite observations in the visible (VIS) spectral region and this was expanded to the near-infrared (NIR) and shortwave infrared (SWIR) spectral ranges as satellite sensor capabilities expanded. The Advanced Very High Resolution Radiometer (AVHRR), Moderate Resolution Imaging Spectroradiometer (MODIS), and Visible Infrared Imaging Radiometer Suite (VIIRS) aerosol products all stem from algorithms making use of these spectral ranges (Torres and Remer, 2013). In parallel to these efforts, measurements in the near ultraviolet (NUV) spectral range also developed during the 1990s. The Total Ozone Mapping Spectrometer (TOMS) and the Ozone Monitoring Instrument (OMI) aerosol products all derive from NUV retrievals (Herman et al., 1997; Torres et al., 2007).

The UV spectral range is dominated by molecular scattering. Insertion of a layer of aerosol disturbs the signal expected by a pure molecular atmosphere, registered by a difference in expected UV reflectance at top-of-atmosphere (TOA) and also by the spectral slope of the UV reflectances (Torres and Remer, 2013). Thus, there are *two* pieces of information available to characterize aerosol in the UV. However, the retrieval is sensitive to *three* parameters: 1) the aerosol loading (AOD); 2) the absorption properties of the aerosol; and 3) the height of the aerosol layer (Torres et al., 1998). While parameters (2) and (3) also play a role in the VIS-SWIR retrieval, the sensitivity is much less than the sensitivity of the loading (Remer et al., 2005). That is why we can assume values for (2) and (3) in the VIS-SWIR retrieval to make a robust retrieval of (1). However, in the UV the three are more equally weighted. Assumptions of one of the three parameters will yield retrievals of the other two, but unfortunately that retrieval is plagued with higher-than-ideal uncertainty. It has been shown, however, that when aerosol layer height (ALH) can be prescribed using either surface-based lidar observations (Torres et al., 2005) or satellite-borne lidar measurements (Jethva et al., 2014), accurate single scattering albedo (SSA) can be derived from NUV satellite observations.

To reduce the uncertainty in the NUV retrieval, one additional piece of information is needed. If a sensor had a broader spectral range, from the NUV to the SWIR, then the VIS-SWIR range

would provide sufficient information for a robust retrieval of spectral AOD. That information could be passed to the UV retrieval, constraining the aerosol loading and allowing robust retrieval of SSA and ALH. Such an idea was tested in Satheesh et al. (2009, 2010) using collocated MODIS and OMI inputs and showed much improved ALH retrieval when compared to lidar measurements although no validation of aerosol absorption was possible. The method was never put into operational production, as MODIS and OMI were on separate platforms and involved in separate missions.

All of the above discussion refers to algorithms making use of multispectral radiance inputs of a primarily scattering signal. Another path to take for aerosol retrieval is to make use of narrow spectral channels in gaseous (specifically Oxygen, O₂) absorption bands. This also allows for retrieval of ALH, and the satellite measurement capability of combined NUV, VIS, NIR, and O₂ radiances (A- and B-bands) was achieved for the first time by the Earth Polychromatic Imaging Camera (EPIC) on the Deep Space Climate Observatory (DSCOVR) at the Lagrangian 1 (L1) point (Marshak et al., 2018). This allowed for the first time the application of an algorithm that simultaneously retrieves NUV AOD and SSA along with ALH at a coarse 18 km resolution (Torres et al., 2025). A similar 3-parameter algorithm was applied to observations by the TROPOspheric Monitoring Instrument (TROPOMI) on the European Sentinel-5 Precursor satellite (Torres et al., 2020a) at a 3.5 km x 5m resolution. The second-generation Cloud Aerosol Imager (CAI-2) sensor on the Greenhouse Observing Satellite (GOSAT-2) includes 339 nm (backward viewing) and 377 nm (forward viewing) near UV channels at 460 m spatial resolution. Although GOSAT-2/CAI-2 near-UV observations spatial resolution is unprecedented, their 40° viewing configuration difference (Hashimoto and Shi, 2020) complicates the applicability of the heritage NUV retrieval approach.

Today an opportunity exists to combine the information from a broad-spectrum instrument that covers the range from 350 nm to 2.25 μm, allowing both the VIS-SWIR and NUV approaches to combine into a single Unified Aerosol Algorithm (UAA). This instrument is the Ocean Color Instrument (OCI) flying on the Plankton, Aerosol, Clouds, ocean Ecosystem satellite (Werdell et al., 2019). OCI is a hyperspectral imaging radiometer with a cross-track swath of 2700 km and a nominal pixel spatial resolution of 1.2 km. To minimize the amount of ocean glint in the images,

OCI performs a 19.9° along-track tilt that occurs at the subsolar point on each orbit. The instrument is pointing aft in the Southern Hemisphere and fore in the Northern Hemisphere. The tilt region follows the sun, appearing exactly over the equator only at the solar equinoxes. In the spectral range from 340 to 896 nm, OCI measures in hyperspectral bands 5 nm wide (full width at half maximum, FWHM) with a 2.5 nm spectral step. In addition, OCI makes measurements in seven discrete bands covering the NIR-SWIR spectral range: 0.94 μm, 1.038 μm, 1.25 μm, 1.378 μm, 1.615 μm, 2.13 μm and 2.26 μm.

The UAA uses bands from the hyperspectral region at 354, 388, 412, 490, 550, 670, 677, 687, and 870 nm, plus the SWIR bands centered near 1.25, 1.378, 1.615, and 2.26 μm. These values are obtained from a weighted average of the two closest OCI nominal bands based on the bands' Relative Spectral Response (RSR) functions. The exceptions are the 677 and 687 nm bands within and adjacent to the O₂ B-band, which are used at their native spectral resolution. OCI's hyperspectral capability also allows independent measures of aerosol layer height using O₂ band techniques. The primary UAA products are spectral AOD, SSA, and ALH.

3 Algorithm Description

Three heritage algorithms provide the basis of the new UAA that is applied to OCI observations. Dark Target (DT) and Deep Blue (DB) come out of the MODIS/VIIRS heritage and make use of the VIS-SWIR wavelengths. NUV represents the TOMS/OMI/TROPOMI heritage and make use of the UV part of the OCI spectrum. Each has been well-documented in the published literature, beginning in the 1990s. We provide short summaries and extensive references of each.

3.1 Scientific theory

The science behind all three heritage algorithms can be described with the radiative transfer equation in reflectance units,

$$\rho^*(\theta_s, \theta_v, \varphi_s - \varphi_v) = \rho_a(\theta_s, \theta_v, \varphi_s - \varphi_v) + \frac{\rho_{sfc} T(\theta_s) T(\theta_v)}{1 - \rho_{sfc} S} \quad (1)$$

where the reflectance at TOA measured by the satellite sensor at a specific wavelength, ρ^* , along a geometrical path through the atmosphere defined by the solar zenith angle, θ_s , satellite view angle, θ_v , and the relative azimuth between the solar and view azimuths, $\varphi_s - \varphi_v$, is equal to the reflectance of the atmosphere itself, defined by the same geometry, $\rho_a(\theta_s, \theta_v, \varphi_s - \varphi_v)$, plus the reflectance from Earth's surface, ρ_{sfc} , attenuated through atmosphere along the downward path from sun to surface, θ_s , and along the upward path from surface to satellite, θ_v . $T(\theta_s)$ is the downward transmission through the atmosphere, $T(\theta_v)$ is the upward transmission and $1 - \rho_{sfc} S$ represents the multiple reflections between atmosphere and the surface where S is the spherical albedo (Vermote et al. 2006; Lenoble and Herman, 2013; also within the Dark Target ATBD Levy et al., 2024). In this form the surface target is of uniform Lambertian reflectance, but the equation can be modified to account for inhomogeneous and anisotropic surfaces.

Each term on the right of Eq.1 depends on the amount and optical properties of the gases and aerosols along the downward and upward paths. If we consider wavelengths primarily in window channels we can ignore or correct for the gaseous absorption. Molecular scattering can be modeled based on the altitude of the surface target. If the surface reflectance can be estimated, then most of the variability in the reflectance reaching the satellite is due to aerosols. The technique used by all three heritage algorithms is to run a radiative transfer code multiple times systematically perturbing the wavelength, geometry and aerosol loading and properties for each run. The result is an array of modeled ρ^* , each linked to a specific satellite viewing and aerosol situation. The heritage algorithms match the satellite-measured ρ^* to the modelled ρ^* , and thus, “back out” the aerosol loading and properties. Heritage sensors such as MODIS, VIIRS, OMI and TropOMI are limited in aerosol information content in their measurements. Therefore, assumptions must be made to constrain some of the aerosol free parameters to retrieve others. Each of the heritage algorithms differ in the wavelength ranges employed and tailor their assumptions to best extract the aerosol information available in their wavelength range. The next sections provide summary descriptions of each heritage algorithm.

3.2 Heritage Dark Target algorithm

The best documentation for the DT algorithm can be found at <https://darktarget.gsfc.nasa.gov/atbd-overview-download> (Levy et al., 2024). DT algorithm was designed to retrieve spectral AOD from MODIS (Remer et al., 2005), has been adapted for VIIRS (Levy et al., 2015; Sawyer et al., 2020) and several geostationary sensors (Gupta et al., 2019; 2024). The algorithm is actually two algorithms, one for aerosols over ocean (Tanré et al., 1997) and one for aerosols over land (Kaufman et al., 1997; Levy et al. 2007ab). Before dividing into either the ocean or land algorithm paths, the mechanics of the retrieval begin with ingesting the satellite image and identifying those pixels inappropriate for an aerosol retrieval. Such pixels include suspended sediments and glint for the over ocean retrieval, bright terrestrial pixels such as deserts for the over land retrieval, and clouds, snow, ice for both ocean and land. These inappropriate pixels are masked from further attention. Then the algorithm organizes the image array into retrieval boxes of a specific size. For example, MODIS inputs of 0.5 km resolution pixels are organized into retrieval boxes of 20x20 pixels or nominally 10 km x 10 km. The measured spectral reflectance of all unmasked pixels within the retrieval box are averaged to produce the mean spectral reflectance that represents that box. The mean reflectance is corrected for gaseous absorption by H₂O, O₃, CO₂, N₂O, CH₄, O₂ and SO₂ (Patadia et al., 2018) and is the input for the actual retrieval (Levy et al. 2013).

The over ocean algorithm makes use of six wavelengths spanning the range of 550 nm to 2.25 μm (Tanré et al., 1997; Remer et al., 2005). A Look Up Table (LUT) is constructed of TOA spectral reflectances for ten single mode aerosol models, four representing particles in the fine mode and six in the coarse mode. Each aerosol model is defined by a single-mode size distribution and complex refractive index. All but one of the models assume spherical particles; one of the six coarse mode models is composed of a mixture of spheroids to represent nonspherical dust (Zhou et al., 2020ab). The LUT assumes a rough ocean surface with windspeeds of 2, 6, 10 and 14 ms^{-1} (Cox and Munk, 1954), water-leaving reflectance in the green wavelength (550 nm) of 0.005, and no water-leaving reflectance at other wavelengths. The retrieval marches through the LUT, combining TOA reflectance from one fine mode and one

coarse mode using a weighting factor to produce a combined TOA reflectance that can be compared with mean measured reflectance, wavelength by wavelength:

$$\rho_{\lambda}^{*}(AOD) = \eta \rho_{\lambda}^{*f}(AOD) + (1 - \eta) \rho_{\lambda}^{*c}(AOD) \quad (2)$$

Here $\rho_{\lambda}^{*}(AOD)$ represents the LUT TOA reflectance at wavelength, λ , for a particular AOD in the LUT, superscripts f and c represent the fine mode and coarse mode, respectively, and η is the mode optical weighting factor (often called fine mode fraction or fine model fraction, FMF). Reflectance without an f or c superscript represents the total reflectance to be compared with the satellite measurement. The average difference between measured reflectance and LUT reflectance is minimized in a least squares sense across all six wavelengths to find the combination of modes and the aerosol loading of each one that best represents the spectral TOA reflectance. The result is an AOD, the two chosen modes, and the mode weighting parameter, η .

The DT over-land algorithm makes use of three wavelengths, one in the blue, one in the red and one in the 2 μm range (Levy et al., 2007ab). The land LUT is constructed using four bimodal aerosol models; three are dominated by the fine mode but differ in absorption properties and one is dominated by the coarse mode. The fine mode-dominated models consist of spherical particles and are fixed by seasonal global maps. The coarse mode-dominated model consists of a mix of spheroids and is global. The greatest challenge in retrievals over land is in constraining the surface. The DT land algorithm uses empirical relationships between blue, red and 2 μm surface reflectance, modified by scattering angle and a measure of surface “greenness”. During the retrieval, the LUT’s Rayleigh scattering component is modified for elevation of the target. Differences between TOA reflectances are minimized in the blue and red wavelengths to obtain AOD and the relative weighting of fine-dominated and coarse-dominated bimodal models that define the spectral dependence of the AOD in the visible, from blue through red.

The contribution of the DT algorithm to UAA is to produce six wavelengths of AOD from 550 nm to 2.25 μm over ocean along with a size distribution model consisting of one fine mode and one coarse mode and the relative weighting between them (η). Over land when surface reflectance is sufficiently dark, the DT algorithm produces AOD in three visible channels, with the other parameters considered to be diagnostics.

3.3 Heritage Deep Blue algorithm

The Deep Blue (DB) algorithm was originally developed to retrieve aerosol properties over bright surfaces, such as deserts and barren areas, thereby enhancing the spatial coverage of aerosol products (Hsu et al., 2004, 2006). This was achieved by primarily utilizing blue wavelengths (412 to 490 nm) at which the contribution of surface reflectance to the top-of-atmosphere signal is significantly lower compared to longer wavelengths, thus providing better sensitivity to aerosols. Since then, DB has been extended to near-global land surfaces (excluding cloud, snow, or ice-covered areas) by adopting a DT-like approach for dark surfaces (Hsu et al., 2013), and to water surfaces through the development of the Satellite Ocean Aerosol Retrieval (SOAR) algorithm (Sayer et al., 2012, 2018). The algorithm suite has been successfully applied to several sensors, including AVHRR (AVHRR; Hsu et al., 2017; Sayer et al., 2017), the Sea-viewing Wide Field-of-view Sensor (SeaWiFS; Hsu et al., 2012), MODIS (Hsu et al., 2013), and VIIRS (Hsu et al., 2019; Lee J et al., 2024), as well as multiple geostationary sensors, enabling the creation of a consistent, long-term aerosol climate data record. Like the DT algorithm, the primary DB product is spectral AOD, with secondary parameters including Ångström exponent and aerosol type.

The DB over-land algorithm uses three different approaches for determining surface reflectance, depending on surface characteristics. First, surface reflectance over bright surfaces, defined as the normalized difference vegetation index (NDVI; Tucker, 1979) less than 0.1, is determined using a minimum reflectance technique. Several years of Rayleigh- and gas-corrected ROA reflectance data, aggregated into 0.1° grids, are used to derive the minimum reflectance in each grid as a function of scattering angle and season. Second, over greener (dark) surfaces (NDVI > 0.1), surface reflectance is estimated using interspectral relationships between visible bands (490 and 670 nm) and a SWIR band ($\sim 2 \mu\text{m}$). Third, over areas where these two approaches show limitations (often bright, heterogeneous areas such as urban or croplands), a hybrid approach is employed combining a predefined bidirectional reflectance distribution function (BRDF) derived at Aerosol Robotic Network (AERONET, Holben et al., 1998) sites within the target domain with the minimum reflectance database at a fixed scattering angle (135°). The primary

wavelengths used for aerosol retrievals are 410 and 490 nm for the bright and hybrid approaches, and 490 and 670 nm over dark surfaces.

The DB land algorithm uses two aerosol optical model sets, one for fine-dominated aerosols and one for mineral dust. A bimodal lognormal size distribution is assumed, with fine-mode AOD fractions of 0.90 and 0.15, respectively, and SSA ranging from 0.89-0.995. The fine-dominated model assumes spherical particles, while the dust model assumes spheroids (Lee J et al., 2017). SSA is predefined by geographic region, season, and AOD to better represent changing aerosol characteristics.

The UAA is based on the VIIRS DB Version 1 over-land algorithm. SOAR is not incorporated, relying solely on DT algorithm for ocean retrievals. Although PACE OCI lacks IR channels, which introduces limitations in detecting smoke and dust, it provides reliable AOD retrieval over land using three visible channels with which DB performs optimally.

3.4 Heritage Near UV algorithm

The NUV spectral region offers unique sensitivity of TOA observations to aerosol extinction and absorption, along with relatively lower land surface albedo over continental dark and desert surfaces. The UV Aerosol Index (UVAI), first defined as a residue parameter in the total column Ozone retrieval from the Nimbus-7/TOMS instrument (Herman et al., 1997), has been proven as an excellent semi-quantitative parameter to identify the presence of UV-light-absorbing aerosols, such as carbonaceous aerosols in smoke plumes and mineral dust.

Importantly, it remains informative over a diverse range of backgrounds including oceans, continents, and bright reflecting backgrounds such as clouds, sea ice, and snow-covered surfaces. The residue represents the spectral contrast in the signal between the two NUV wavelengths after the removal of Rayleigh scattering effects following the Lambertian Equivalent Reflectivity (LER) approach adopted in the early 1990s. Since most of the signal in this residue parameter is attributed to the aerosol effects, it was termed as UVAI and formulated as

$$UVAI = -100 \left[\log \left(\frac{I_{sm}}{I_{lm}} \right)_{meas} - \log \left(\frac{I_{sc}}{I_{lc}} \right)_{calc} \right] \quad (3)$$

where, I_{sm} and I_{lm} are the measured TOA radiances at a shorter and longer wavelength, respectively, from the satellite sensor and I_{sc} and I_{lc} are the calculated radiance following the LER approach with the longer wavelength as a reference. The UVAI varies between negative numbers, down to about -1, generally associated with small size non-absorbing aerosols, around zero for most clouds, and positive values for UV-absorbing aerosols. The UVAI magnitude in the presence of absorbing aerosols depends mainly on the AOD, SSA, and ALH (Torres et al., 1998). Double-digit UVAI values are typically observed in the aftermath of pyro-Cb events (Fromm et al, 2010) when optically thick carbonaceous aerosol layers reach the upper troposphere and stratosphere, as documented in the aftermath of the 2017 British Columbia pyroCb event (Torres et al., 2020b). A UVAI-like signal can be generated by surface types with spectrally varying LER such as deserts, and the remote ocean where pure water UV absorption effects (Lee Z et al., 2015) generate positive UVAI values (up to about 1). To account for these surfaces, an empirical correction was introduced that subtracts surface LER, based on long-term monthly climatology, from the calculated LER before deriving UVAI. In recent years, further refinements to the UVAI have been made to account for the angular scattering effects of water clouds. Large negative UVAI over seasonally occurring cloudy skies, such as southern Africa and the southeastern Atlantic Ocean, necessitated this refinement. The new formulation of UVAI and its regional and global application are described in Torres et al., (2018).

By leveraging the strong sensitivity to aerosols, coupled with lower surface albedo, a two-channel NUV algorithm was developed and applied to the TOMS sensor aboard Nimbus-7 and EarthProbe platforms to deduce for the first time the global distribution of UV-absorbing aerosols over the oceans and the continents (Torres et al., 2002). Radiative transfer simulations revealed that the TOA observations between the 340 to 380 nm spectral region are primarily sensitive to the three aerosol parameters: AOD, SSA, and ALH. The dependence of the NUV radiances to ALH stems from the radiative interactions between aerosols and molecular scattering; elevated layers of aerosols increase the likelihood of enhanced aerosol absorption caused by Rayleigh scattering beneath these aerosols. When constrained with an aerosol model and ALH, the NUV algorithm retrieves AOD and SSA simultaneously at the longer wavelength (either at 380 nm or 388 nm, depending on the sensor). An improved version of the algorithm

was also designed and applied to the long-term record of the Ozone Monitoring Instrument (OMI) (Torres et al., 2007, Jethva et al., 2011; Torres et al., 2018). The record has been further extended with observations from the DSCOVR-EPIC (Ahn et al., 2021), and more recently from the Sp5-TROPOMI (Torres et al., 2020a), providing nearly 40 years of AOD and SSA.

OCI's hyperspectral capability allows continuation of NUV aerosol retrievals at much higher spatial resolution than its predecessor sensors. The strength and unique philosophy of the UAA further advances the NUV retrieval capability by providing a constraint on the total AOD first retrieved at the visible wavelengths, followed by its conversion to the UV (354 and 388 nm). As noted previously, the TOA signal at the two NUV wavelengths exhibited a marked sensitivity to AOD, SSA, and ALH, which is further illustrated in Fig. 1 below. The theoretical RT simulations are shown for a fine mode dominated carbonaceous aerosol model for varying imaginary part of the refractive index (or SSA) and ALH at two distinct AODs. The grey (blue) lines connect simulations for varying ALH values (SSA values) at a fixed value of SSA (ALH). This sensitivity of TOA radiances and their color ratio, when constrained with columnar AOD, forms the physical basis for simultaneously retrieving the SSA/ALH pair from OCI observations. Such an approach was first demonstrated in Satheesh et al. (2009) employing MODIS-retrieved AOD to constrain the OMI retrieval, freeing OMI from making an *a priori* assumption of ALH and allowing rather a more direct retrieval of SSA and ALH. The suggested approach was successfully demonstrated over the tropical Atlantic and Arabian Sea oceanic regions. OCI presents a perfect opportunity to employ such an approach on a daily global basis. UAA aims to demonstrate the synergy of NUV and VIS to SWIR observations to derive a comprehensive suite of aerosol products that was either very limited or non-existent in the past.

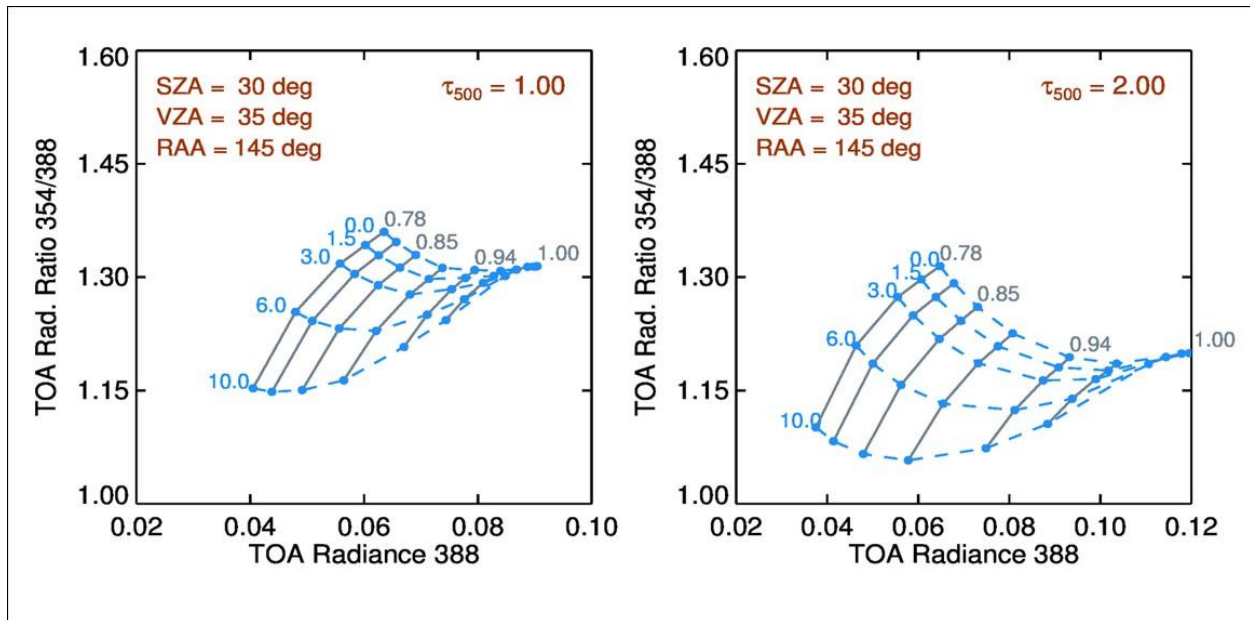


Figure 1 Radiative transfer calculations of TOA radiances and color ratio at NUV wavelengths of 354 nm and 388 nm of an assumed carbonaceous aerosol model. The results are shown for two distinct AODs (500 nm) of 1.0 (left) and 2.0 (right). Grey lines (blue lines) connect simulations for varying ALH values (SSA values) at a fixed value of SSA (ALH).

3.5 Merging the three heritage algorithms

The UAA takes the three heritage algorithms and combines them into a flow structure ingesting OCI data to produce aerosol parameters. The main purpose of the DT and DB heritage algorithms is to produce outputs of cloud-cleared spectral reflectances, AOD, and η that the NUV subroutine will ingest and use to constrain their heritage retrieval. Additionally, the NUV algorithm benefits from DT and DB cloud masking traditions and uses η to choose between dust and smoke models in the NUV LUTs.

Several innovations have been implemented into the UAA code. Over land the DT and DB retrievals are combined with new logic and the VIS-SWIR spectral AODs are extrapolated to the UV. The extrapolation is done internally in the DT ocean algorithm but is done externally over land using a Machine Learning (ML) model. DT ocean has also implemented its own internal algorithm for retrieving SSA, as an alternative to the near UV method. Finally, UAA has added an O₂ B-band retrieval for aerosol layer height. These innovations and others are described in detail in the following sections.

We present the overall structure and flow of the UAA in Fig. 2. Subroutines arising from the NUV heritage are in light orange, from DT in purple, from DB in dark blue. Green indicates subroutines with no heritage that are unique to the UAA algorithms. The output is captured in light blue. The UAA code reads in OCI reflectances and processes these to match the wavelength expectations of the LUTs of the three heritage traditions. Immediately the code calculates the UVAI, which requires no cloud masking and provides valuable first looks of aerosol events and climatology.

After the UVAI is calculated the subroutine diverges between over-land and over-ocean retrievals. This requires an ancillary land/ocean data base. If the retrieval is over ocean, the DT ocean subroutine is invoked, which requires nine spectral reflectances. Within the subroutine the DT ocean cloud mask (Martins et al., 2002; Remer et al., 2012) is applied and the heritage algorithm proceeds with a few modifications described in Section 3.7.1. The outputs from the DT ocean algorithm (AOD in the UV-SWIR, η and the cloud cleared reflectances) are made available to the near UV subroutine and also output in the final product. The DT ocean algorithm continues to perform an independent retrieval of SSA, shown in Fig. 2 and described in Section 3.7.2. The DT SSA is output in the final product.

If the retrieval will be over land both the DT and DB subroutines are invoked. Each proceeds as described above, with several modifications implemented that adapt the heritage code to the OCI configuration described in Section 3.7.3. Clouds are masked and both DT and DB output AOD in three visible wavelengths. Continuing over land, the AOD output from DT and DB are merged to produce a single value of AOD, labeled as UAA AOD in Figure 2. The VIS UAA AODs and the cloud-cleared reflectances over land are passed to the near UV subroutine. The near UV subroutine also requires AOD in the UV. The ML model used for spectral extrapolation for this is shown in a green box in Figure 2 and described in Section 3.7.4. Now the NUV algorithm has everything to perform its retrieval; specific changes of the NUV algorithm for the UAA are described in Section 3.7.5.

The UAA also includes a module for deriving AOD above clouds (Section 3.7.6) and another for Oxygen B band retrievals of ALH (Section 3.7.7) that resides outside of the main flow of the

algorithm. This routine ingests OCI reflectances in two bands and uses this information to derive ALH independently of the near UV subroutine.

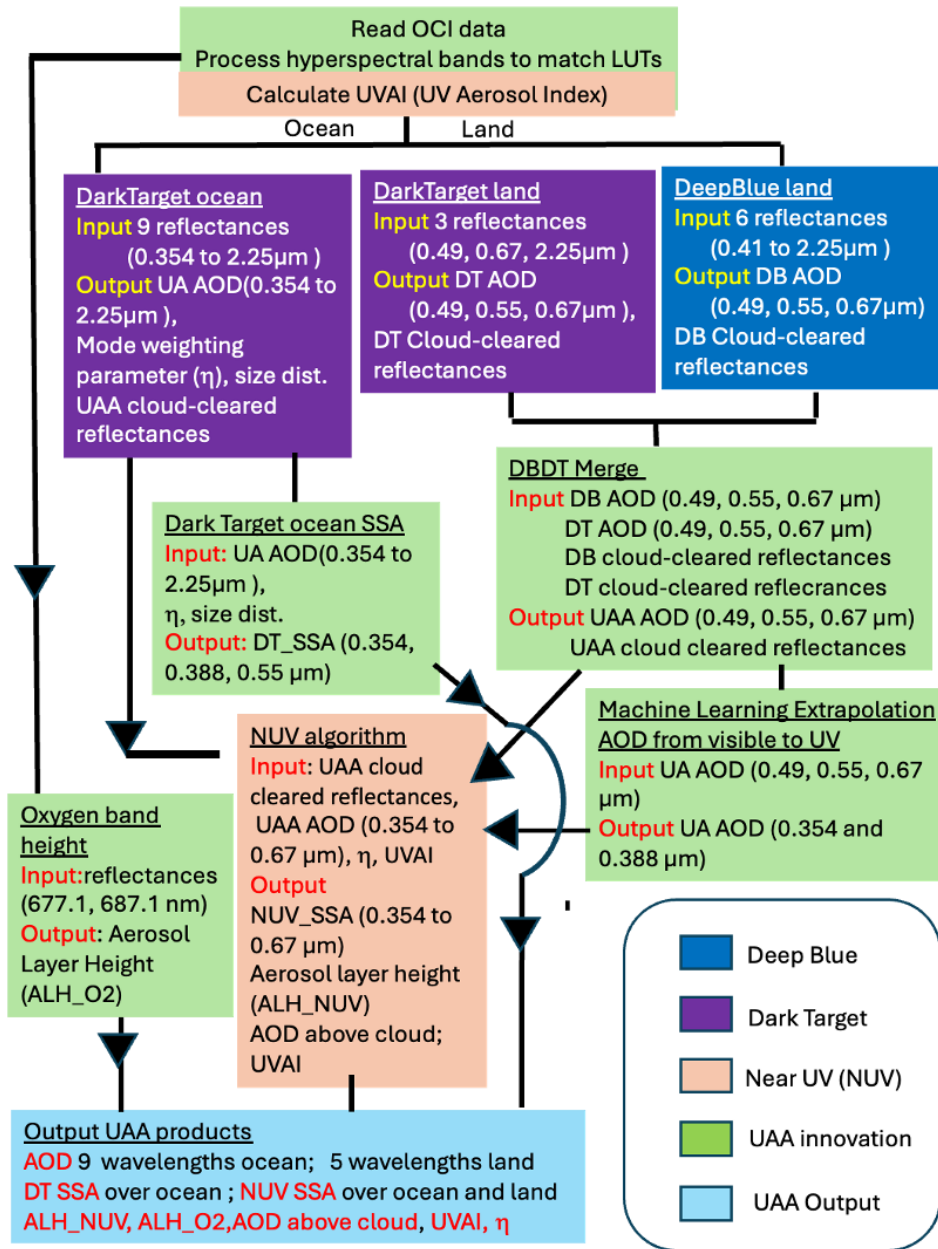


Figure 2. Flow chart showing over all structure of the UAA algorithm, from ingest of OCI data to output of UAA products. Heritage algorithms and specific UAA innovations are denoted by color.

The final output of UAA includes AOD in nine wavelengths over ocean and five wavelengths over land, two independent spectral SSA products, and two ALH products. Other output products

include the DT ocean mode weighting parameter (η) that is a robust physical measure of the FMF of the AOD at 550 nm μm (Remer et al., 2005), the AOD above clouds that can be combined with clear sky AOD to form a combined all-sky AOD product, and UVAI at two spatial resolutions. The full list of output parameters is tabulated and described Section 3.7.

3.6 Algorithm input and output variables

The algorithm inputs data from three sources: PACE OCI Level 1B data, the Goddard Global Modeling and Assimilation Office (GMAO) ancillary data and an external land/water mask. The data source, parameter name, long name and unit are given in Table 1.

Table 1. UAA algorithm input data

Source	Name	Long name	Unit
PACE L1B	latitude	Latitudes of pixel locations	degrees_north
	longitude	Longitudes of pixel locations	degrees_east
	solar_azimuth	Solar azimuth angle at pixel locations	degrees
	solar_zenith	Solar zenith angle at pixel locations	degrees
	sensor_zenith	Sensor zenith angle at pixel locations	degrees
	sensor_azimuth	Sensor azimuth angle at pixel locations	degrees
	Height	Terrain height at pixel locations	meters
	Watermask	Watermask	-
	Time	Time	seconds since start of day (UTC)
	SWIR_wavelength	Band center wavelengths for SWIR bands	nm
	blue_wavelength	Band center wavelengths for blue CCD	nm
	red_wavelength	Band center wavelengths for red CCD	nm
	SWIR_solar_irradiance	Mean extraterrestrial solar irradiance at 1 astronomical unit for the wavelengths of the SWIR wavelengths	$\text{W m}^{-2} \mu\text{m}^{-1}$
	blue_solar_irradiance	Mean extraterrestrial solar irradiance at 1 astronomical unit for the wavelengths of the blue CCD	$\text{W m}^{-2} \mu\text{m}^{-1}$
	red_solar_irradiance	Mean extraterrestrial solar irradiance at 1 astronomical unit for the wavelengths of the red CCD	$\text{W m}^{-2} \mu\text{m}^{-1}$
	rhot_SWIR	Top of Atmosphere SWIR Band Reflectance	-

	rhot_blue	Top of Atmosphere Blue Band Reflectance	-
	rhot_red	Top of Atmosphere Red Band Reflectance	-
GMAO	GEOS.it.asm.asm_inst_1hr_glo_L576x361_slv		
	U10M	10-meter eastward wind	ms ⁻¹
	V10M	10-meter northward wind	ms ⁻¹
	TQV	total precipitable water vapor	kg m ⁻²
	TO3	Total column ozone	Dobsons
	TS	Surface skin temperature	K
External	landmask_GMT15ARC.nc		
	watermask	Land/water mask	-

The UAA produces two Level 2 output files, one at native resolution of the OCI (nominally 1.2 km), and the other in 7x7 grid boxes (nominally 8.4 km). The 1.2 km file holds only a fine resolution UVAI, plus geolocation data and some diagnostics. This is file PACE/OCI/L2/UVAI_UAA/3.1 for Version 3.1. The 7x7 product holds all of the other parameters plus their geolocation, geometry, diagnostics and quality flags. This is file PACE/OCI/L2/AER_UAA/3.1.

The parameter lists are given here:

Table 2a. Parameter list for nominal 1.2 km by 1.2 km file PACE/OCI/L2/UVAI_UAA/3.1
1272 cross-track pixels per granule.

Group/Variable	Dimensions	Units	Notes
Geolocation Data			
longitude	(lines,pixels)	degrees	-180° to 180°
latitude	(lines,pixels)	degrees	-90° to 90°
Geophysical_data			
NUV_AerosolIndex	(lines,pixels)	unitless	NUV Retrieved Aerosol Index (0.354-0.388 pair) at native 1.2 km resolution
NUV_Residue	(lines,pixels)	unitless	NUV Retrieved LER based Aerosol Index (0.354-0.388 pair) at native 1.2 km resolution
NUV_Reflectivity	(lines,pixels,2)	unitless	NUV Retrieved LERs for 0.354 and 0.388 μm, individually, at native 1.2 km resolution

Table 2b. Parameter list for nominal 8.4x8.4 km file PACE/OCI/L2/AER_UAA/3.1
181 cross-track pixels per granule.

Group/Variable	Dimensions	Units	Notes
Geolocation Data			
longitude	(lines,pixels)	degrees	-180° to 180°
latitude	(lines,pixels)	degrees	-90° to 90°
solar_zenith_angle	(lines,pixels)	degrees	0° to 180°
solar_azimuth_angle	(lines,pixels)	degrees	-180° to 180°
sensor_zenith_angle	(lines,pixels)	degrees	0° to 180°
sensor_azimuth_angle	(lines,pixels)	degrees	-180° to 180°
Geophysical_data			
Land_Sea_Flag	(lines,pixels)	unitless	Land_Sea_Flag (0 = Ocean, 1 = Land)
Aerosol_Optical_Depth	(lines,pixels,9)	unitless	AOD at 0.354, 0.388, 0.490, 0.550, 0.673, 0.865, 1.24, 1.61 and 2.25 μm
Optical_Depth_Ratio_Small_Ocean_used	(lines,pixels)	unitless	Fraction of AOD (at 0.55 micron) contributed by fine mode
Mean_Gas_Corrected_Reflectance	(lines,pixels,7)	unitless	Mean gas-corrected reflectance of pixels at 0.490, 0.550, 0.673, 0.865, 1.24, 1.61 and 2.25 μm
Mean_Reflectance	(lines,pixels,2)	unitless	Mean reflectance (not corrected for gas) of pixels at 0.354 0.388 μm
DT_AerosolSingleScattAlbedo	(lines,pixels,3)	unitless	Single scattering Albedo from Dark Target ocean subroutine at 0.354, 0.388 and 0.550 μm
DT_AerosolLayerHeight	(lines,pixels)	km	DDT Retrieved Aerosol Layer Height (1.5, 3, 6, 10 km). DIAGNOSTIC. Use NUV_AerosolLayerHeight for science applications
Aerosol_Cld_Fraction_Land_Ocean	(lines,pixels)	unitless	Diagnostic
NUV_AerosolIndex	(lines,pixels)	unitless	NUV Aerosol Index (0.354-0.388 pair) at 7 x7 pixel resolution
NUV_AerosolLayerHeight	(lines,pixels)	km	In km
NUV_AerosolSingleScattAlbedo	(lines,pixels,5)	unitless	NUV Retrieved Aerosol Single Scattering Albedo at 0.354, 0.388, 0.490, 0.550, 0.673 micron
NUV_RadiativeCloudFraction	(lines,pixels)	unitless	DIAGNOSTIC. NUV derived Radiative Equivalent Cloud Fraction at 0.388 μm
NUV_Residue	(lines,pixels)	unitless	DIAGNOSTIC

NUV_Reflectivity	(lines,pixels,2)	unitless	NUV Lambertian Equivalent Reflectivity (LER) at 0.354 and 0.388 μm
NUV_CloudOpticalDepth	(lines,pixels)	unitless	NUV Retrieved Cloud Optical Depth at 0.388 μm
NUV_AerosolOpticalDepthOverCloud	(lines,pixels,3)	unitless	NUV Retrieved Aerosol Optical Depth Over Cloud at 0.354, 0.388, 0.550 μm
NUV_AerosolCorrCloudOpticalDepth	(lines,pixels)	unitless	NUV Retrieved Aerosol Corrected Cloud Optical Depth at 0.388 μm
NUV_AerosolOpticalDepthOverCloudVsHeight	(lines,pixels,3,5)	unitless	NUV Retrieved Aerosol Optical Depth Over Cloud for 0.354, 0.388, 0.550 micron at 5 levels (3, 6, 9, 12, 15 km)
NUV_AerosolCorrCloudOpticalDepthVsHeight	(lines,pixels,5)	unitless	NUV Retrieved Aerosol Corrected Cloud Optical Depth for 0.388 micron at 5 levels (3, 6, 9, 12, 15 km)
NUV_FinalAlgorithmFlagsACA	(lines,pixels)	unitless	NUV Final Algorithm Flags for Above-cloud retrievals
NUV_UncertaintyACAODToSSA	(lines,pixels,2)	unitless	NUV derived percent uncertainty in COD due to change in SSA
NUV_UncertaintyCODToSSA	(lines,pixels,2)	unitless	NUV derived percent uncertainty in Aerosol-corrected COD due to plus/minus 0.03 change in SSA
Quality_flag_Aerosol_Optical_Depth	(lines,pixels)	unitless	Land=0 Ocean=0,1,2,3
Quality_flag_SingleScattAlbedo	(lines,pixels)	unitless	Quality_flag_SingleScattAlbedo 0,1,2,3
O2B_AerosolLayerHeight	(lines,pixels)	km	O2-B Retrieved Aerosol Layer Height

3.7 UAA creative innovations

The UAA is based on three heritage algorithms but includes several creative innovations. Some of these innovations are to adapt heritage algorithms for OCI inputs or modify the algorithms to make use of the synergy of running the three algorithms together; others lead to new products, unique to the UAA.

3.7.1 Adapting DT and DB heritage to OCI sensor characteristics

New DT and DB LUTs have not been created for UAA. Rather than adjusting the LUTs, OCI bands are chosen and contiguous bands averaged to match the discrete wavelength bands

used by VIIRS. Thus, the DT and DB LUTs used by the algorithms to process VIIRS inputs are used for UAA with no alteration.

The heritage DT algorithm inputs small chunks of 2-dimensional arrays of a sensor's native resolution and then uses that native resolution for cloud, snow, ice, glint, sediment and bright land surface masking. The masking is done by reading in an entire granule, one chunk at a time. Then the algorithm calculates the mean reflectance of the remaining unmasked good pixels representative of the array (Remer et al., 2012). The mean reflectance of this array or retrieval box moves forward in the retrieval to obtain aerosol products. The size of the array is sensor specific. The DB algorithm employs a different approach than the heritage DT algorithm. DB performs bad pixel masking (cloud, snow, etc.) at the sensor's native resolution and conducts retrievals at the pixel level. After obtaining retrievals at this native resolution, the algorithm then aggregates these pixel-level results to the reported spatial resolution.

For MODIS, DT used 20x20 arrays of 0.5 km native pixels because these matched the width of the MODIS scan mirror in the along-track direction. Here we do not need to consider width in pixels of a scan mirror as OCI uses a single telescope to make its cross-track scan (Meister et al., 2024). Instead, we choose a box size more comparable to DT VIIRS's finer resolution box and arrange OCI native pixels into retrieval boxes of 7x7 pixels of 1.2 km. All three heritage algorithms follow the DT tradition and organize their retrievals into these 7x7 pixel retrieval boxes. In addition to the UVAI produced in the 7x7 pixel box, the algorithm also produces the UVAI at OCI native resolution and makes that available in a separate data file.

The other modification needed by DT for OCI is to find substitutions for the missing thermal infrared (TIR) wavelengths that all DT predecessor sensors offered but OCI does not. TIR wavelengths are used for both snow/ice and cloud masking. For snow masking, without a temperature sanity check, the land snow mask will erroneously identify snow pixels throughout the tropics. The problem is solved by using ancillary input reanalysis data (Global Modeling and Assimilation Office - GMAO) for skin temperature. For cloud masking by DT, the TIR test is a very minor contributor to the DT cloud mask that relies mostly on spatial variability using VIS channels, coupled with a 1.375 μm band for cirrus detection. The OCI UAA cloud mask over

ocean and DT land retrievals simply drops the TIR test. This will introduce some isolated cloud contamination and mildly increase uncertainty in the product but should not be a driving factor in the overall uncertainty of the retrieval. The loss of the TIR wavelengths is more serious for DB, especially over bright deserts where heritage DT does not make a retrieval and where the DT cloud mask has never been applied or tested.

Despite this limitation, the adapted DB algorithm proceeds with aerosol retrievals without implementing a direct substitute for the TIR tests. In the VIIRS DB algorithm TIR measurements were also utilized for aerosol type classification. Currently, no direct replacement for TIR observations exists within the OCI framework, resulting in some sacrifice of algorithm performance. To minimize this degradation, more stringent quality assurance tests were implemented in the retrieval process. The current implementation demonstrates adequate performance for operational applications, though future research may explore alternative methodologies to compensate for the absence of TIR information.

3.7.2 Extending DT for a SSA retrieval over ocean

The main innovation of the UAA is to constrain the AOD in the UV spectrum so that retrievals making use of that wavelength band are free to retrieve absorption parameters (SSA) and ALH (as an optical centroid height). Over land, the AOD in the UV is extrapolated from retrievals made by the VIS-SWIR subroutines using a ML model that will be described in Section 3.7.4. Over ocean, the DT algorithm is modified to perform this extrapolation internally, as the DT over ocean algorithm is sufficiently sensitive to spectral extinction for an extrapolation to succeed. In fact, the extrapolation leads to a full DT aerosol retrieval using UV wavelengths that produce both a value of AOD and SSA in the UV over ocean.

To accomplish the DT retrieval in the UV, the DT LUT is extended for two new wavelengths at 354 and 388 nm. Using the previously defined size parameters from the heritage LUT, each of the original ten modes is expanded into four different models by varying the imaginary part of the refractive index for each of the two UV wavelengths. The real part of the refractive index is kept the same value from the heritage blue wavelength.

Table 3. Expanded aerosol optical property assumptions for Dark Target retrieval over ocean. Models 1 – 9 are spherical. Model 10 is spheroidal.

Fine Particles

	0.354 μm	0.388 μm	r_g	s	r_{eff}
1	A: 1.45-0.0035i B: 1.45-0.0078i C: 1.45-0.00607i D: 1.45-0.0211i	A: 1.45-0.0035i B: 1.45-0.0075i C: 1.45-0.00515i D: 1.45-0.0161i	0.07	0.40	0.10
2	A: 1.45-0.0035i B: 1.45-0.0078i C: 1.45-0.00663i D: 1.45-0.0230i	A: 1.45-0.0035i B: 1.45-0.0075i C: 1.45-0.00619i D: 1.45-0.0193i	0.06	0.60	0.15
3	A: 1.40-0.0020i B: 1.40-0.0078i C: 1.40-0.00386i D: 1.40-0.0134i	A: 1.40-0.0020i B: 1.40-0.0075i C: 1.40-0.00391i D: 1.40-0.0122i	0.08	0.60	0.20
4	A: 1.40-0.0020i B: 1.40-0.0078i C: 1.40-0.00234i D: 1.40-0.00814i	A: 1.40-0.0020i B: 1.40-0.0075i C: 1.40-0.00236i D: 1.40-0.00736i	0.10	0.60	0.25

Coarse Particles

	0.354 μm	0.388 μm	r_g	s	r_{eff}
5	A: 1.35-0.001i B: 1.35-0.0065i C: 1.35-0.00259i D: 1.35-0.009i	A: 1.35-0.001i B: 1.35-0.0056i C: 1.35-0.00237i D: 1.35-0.00739i	0.40	0.60	0.98
6	A: 1.35-0.001i B: 1.35-0.0065i C: 1.35-0.00289i D: 1.35-0.0101i	A: 1.35-0.001i B: 1.35-0.0056i C: 1.35-0.00267i D: 1.35-0.00832i	0.60	0.60	1.48
7	A: 1.35-0.001i B: 1.35-0.0065i C: 1.35-0.00332i D: 1.35-0.01161i	A: 1.35-0.001i B: 1.35-0.0056i C: 1.35-0.00296i D: 1.35-0.00923i	0.80	0.60	1.98
8	A: 1.53-0.000i B: 1.53-0.0065i C: 1.53-0.00164i D: 1.53-0.009i	A: 1.53-0.000i B: 1.53-0.0056i C: 1.53-0.00150i D: 1.53-0.010i	0.60	0.60	1.48
9	A: 1.53-0.000i B: 1.53-0.0065i C: 1.53-0.00114i D: 1.53-0.011i	A: 1.53-0.000i B: 1.53-0.0056i C: 1.53-0.00101i D: 1.53-0.010i	0.50	0.80	2.50
10	A: 1.53-0.0040i B: 1.53-0.0071i C: 1.53-0.0102i D: 1.53-0.0132i	A: 1.53-0.0032i B: 1.53-0.0063i C: 1.53-0.0094i D: 1.53-0.0102i	0.5	0.6	1.23

Table 3 shows the values of complex refractive index for each UV wavelength, the geometric mean (r_g), geometric standard deviation (σ) and effective radius (r_{eff}) of the lognormal size distribution. Models 1 – 9 are assumed spherical with their LUT calculations performed using Mie code (Remer et al., 2005), while Model 10 is nonspherical and reserved for dust retrievals (Zhou et al., 2020b). The LUT calculations in the two new UV channels are done for each of the four imaginary indices, at four different ALH (1.5, 3, 6, and 10 km) and at four surface wind speeds (2, 6, 10, and 14 ms^{-1}).

The DT UAA retrieval over ocean begins the same as the heritage DT algorithm, using the VIS to SWIR bands to retrieve AOD at 550 nm, one fine mode, one coarse mode and η from Eq. 2. The surface windspeed is provided by ancillary data. The retrieved size distribution defines a unique spectral dependence for AOD, allowing for extrapolation of the AOD to the two UV wavelengths. The extrapolation does not make use of the Ångström Exponent and can curve in log-log space (Eck et al., 1999). The retrieved bimodal size distribution limits the choice of spectral absorption in the UV to one of four possibilities (A, B, C or D) in Table 3, representing a dynamic range of UV aerosol absorption characteristics taken from measurements and appearing in the literature. The models cover a range of aerosol types from desert dust to carbonaceous aerosol types (Krotkov et al. 2005; Dinar et al., 2007; Mogo et al., 2012; Wagner et al., 2012; Rocha Lima et al., 2014, 2018). Note that the fine and coarse mode imaginary part of the refractive index of any of the four possible models are linked but not the same. This leaves only two free parameters remaining, the UV spectral absorption model (A, B, C or D), plus the aerosol layer height. The retrieval minimizes the difference between the measured and LUT values of reflectances in the two UV wavelengths for each of the four aerosol layers, then minimizes again to find the layer with the smallest error to provide SSA at 354 and 388 nm.

The SSA is extrapolated to 550 nm using a multiple regression model parameterized by the Ångström Exponent and the difference between SSA at 388 354 nm, based on the data base presented as Table 3 in Kayetha et al. (2022). The dependency on Ångström Exponent distinguishes between dust-like aerosol and carbonaceous aerosol, and the spectral dependence on SSA in the UV further refines the projection into the visible. The result of the UAA DT retrieval over ocean are the AOD at 9 wavelengths from 354 nm to 2.25 μm , the η parameter that

is an indication of aerosol FMF, and SSA at 354, 388, and 550 nm. The ALH is also reported but is considered a diagnostic of the retrieval and not a validated physical parameter.

In Section 5.1 we demonstrate the DT SSA in two case studies, where it looks promising, but its quality is not consistent. Because currently we cannot fit reasonable error bounds on the DT SSA, we are treating the product as a diagnostic for the DT retrieval over ocean, and we are recommending users to not use the product for scientific purposes. A more traditional method of obtaining SSA is made by directly adapting the NUV algorithm to OCI inputs and is described in Section 3.7.5. Validation for this NUV product is shown in Section 5.4.

3.7.3 DT/DB merge over land

Unifying the retrieval of AOD over land requires a merge of the DT and DB outputs. Previous attempts of creating a DT/DB merge were based on assumptions of each algorithm's strengths and weaknesses, using the Normalized Difference Vegetation Index (NDVI) as a guide (Sayer et al., 2014). The problem with this assumption is that it bases the decision only on surface cover and ignores all the other aspects of a retrieval. Local cloud cover, topography, aerosol types etc. may also contribute to aerosol retrieval uncertainty causing one retrieval to perform better than another.

For UAA we base the merge on validation statistics rather than surface cover type. DT and DB AOD at 550 nm from MODIS and VIIRS were collocated with AERONET Level 2 observations (Holben et al. 1998; Giles et al., 2019) using data from March 2012 through November 2020. The only data kept were situations when all three methods reported AOD simultaneously. The mean bias of both DT and DB against AERONET was calculated at each AERONET station, then the difference in absolute bias of DT was subtracted from the absolute bias of DB and plotted for each AERONET station globally in Fig.3. Differences marked as blue indicate that DB has smaller absolute bias than DT, and the reverse is true for differences marked as red.

There are regional trends where each of the two land retrievals have historically shown smaller biases against AERONET. DB outperforms DT in the North American west, the African Sahel, the Iberian Peninsula and much of the Middle East and eastern Asia. Many but not all of these

places are typified by drier vegetation and lower NDVI, as expected previously (Sayer et al., 2014). DT seems to hold an advantage in the North American east, northern South America, southern Africa, southeast Asia and much of Europe, some of which has higher NDVI, but not all. Given the map of Fig. 3, broad regional areas (also shown in Fig. 3) were drawn to identify which algorithm would take precedence in the UAA retrieval. The logic of the merge is as follows:

- If neither DT nor DB produce a retrieval, all outputs in the green DBDT box of Fig. 2 are set to fill values.
- If DT produces a high quality retrieval and DB does not, then the UAA will move forward with the DT result.
- If DB produces a high quality retrieval and DT does not, then the UAA will move forward with the DB result.
- If both algorithms produce high quality retrievals, the UAA will use the AOD values from DT only in areas in which DT has precedence, as denoted by red rectangles in Fig.3 and defined here,
 - a. $-30^{\circ} < \text{Latitude} < 45^{\circ}$ and $-96^{\circ} < \text{Longitude} < -58^{\circ}$
 - b. $45^{\circ} < \text{Latitude}$ and $-20^{\circ} < \text{Longitude} < 5^{\circ}$
 - c. $35^{\circ} < \text{Latitude}$ and $5^{\circ} < \text{Longitude} < 36^{\circ}$
 - d. $\text{Latitude} < 3^{\circ}$ and $5^{\circ} < \text{Longitude} < 52^{\circ}$
 - e. $-10^{\circ} < \text{Latitude} < 30^{\circ}$ and $82^{\circ} < \text{Longitude} < 112^{\circ}$
 - f. $-10^{\circ} < \text{Latitude} < 19^{\circ}$ and $112^{\circ} < \text{Longitude} < 155^{\circ}$
 - e. $-30^{\circ} < \text{Latitude} < 15^{\circ}$ and $145^{\circ} < \text{Longitude} < 160^{\circ}$

Thus, outside of these red boxes, if DB makes a retrieval, it will take precedence.

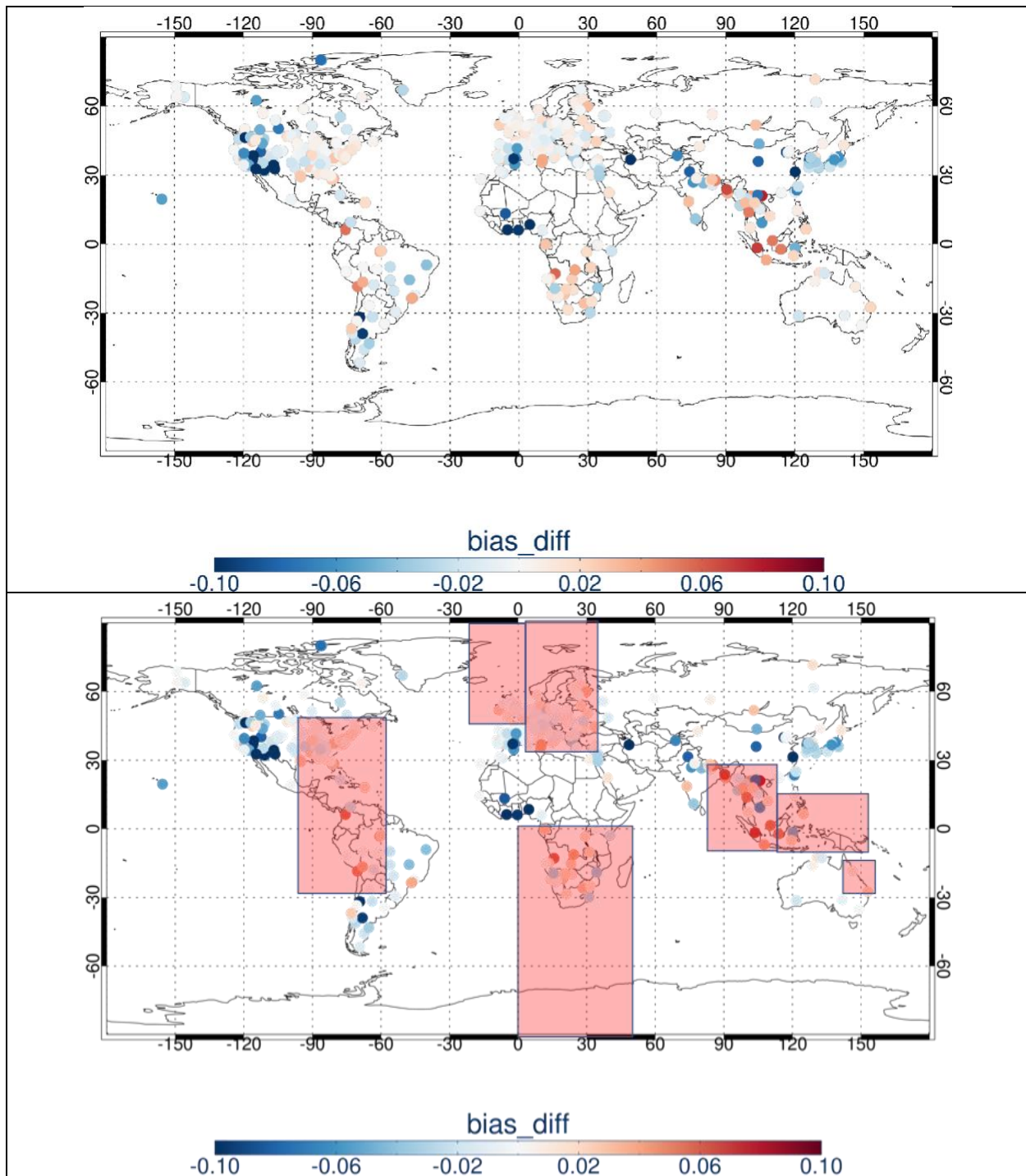


Figure 3. Absolute mean bias of AOD at 550 nm between Deep Blue (DB) retrieved values and AERONET observations minus the same but between Dark Target (DT) retrieved values and AERONET measurements. Negative values indicate that the DB bias is smaller than the DT bias, and vice versa for positive values. Thus, blue dots (top) identify AERONET stations where DB outperforms DT, and red dots identify where DT outperforms DB. Broad regions (bottom) colored red identify where DT will take precedence in the UAA.

3.7.4 Extrapolation of AOD to the UV over land

Over ocean, there is sufficient spectral information retrieved using the VIS-SWIR retrieval to extrapolate AOD into the UV spectral range, but over land the DB and DT retrievals are much more limited. The complexity of the land surface introduces too much uncertainty into the retrievals for robust spectral information to be recovered. Still, the UAA requires AOD in the UV spectral range to constrain the retrieval, making extrapolation a necessity.

The classical method of making a spectral AOD extrapolation is to use the first-order Ångström exponent. This assumes linearity in log-log space for the entire spectral range. Using AERONET AOD measurements at a long-term single location, Alta Floresta, we demonstrate the inadequacy of the linear extrapolation of the AOD into the UV. The extrapolations make use of three of AERONET's visible wavelengths that are similar to those retrieved by the Dark Target algorithm, nominally 440, 500, and 675 nm. The extrapolated AOD at 380 nm is compared with AERONET's measured value. The results are depicted by the red and blue dots/regression lines in Fig. 4; the extrapolated values of UV AOD stray from the 1:1 line even for moderate AOD values and substantially overestimate AOD as aerosol loading increases.

The problem with Ångström exponent extrapolations is that spectral AOD is not linear in log-log space (Eck et al., 1999). To deal with the nonlinearity, Satheesh et al. (2009), in a prototype to the UAA, used an empirical correction in the form of the weighted arithmetic difference between AOD at 470 and 870 nm. That correction was developed at a limited number of AERONET island stations and meant for over ocean retrievals. For the UAA extrapolation over land, we need a different approach, and because Eck et al., (1999) describe the spectral dependence of AOD as a quadratic in log-log space, we explored a quadratic extrapolation. The green points/regression line of Fig. 4 show the results of extrapolating into the UV from the visible using a quadratic fit. From that figure we see that the quadratic extrapolation matches the measurements much better than the linear ones, and if there were no other options we would have pursued a more universal quadratic fit from multiple AERONET stations worldwide. However, Machine Learning (ML) offers another option.

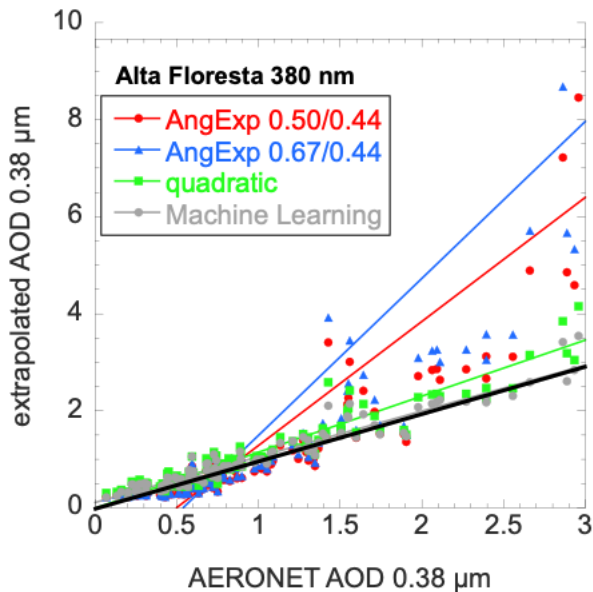


Figure 4. AOD at 380 nm extrapolated from AERONET observations of AOD at 440, 500, and/or 675 nm compared with AERONET measurements of AOD at 380 nm at the Alta Floresta site covering the period 1993 through 2020. Each point represents the average of 1000 observations, after the data was sorted by AOD at 500 nm. Shown are estimates of AOD at 380 nm using two Ångström Exponents (red and blue), each calculated from different pairs of visible wavelengths, the estimates from a quadratic fit (green) and estimates from a Machine Learning model (gray). The thick black solid line is the 1:1 line.

We develop a ML model using VIIRS and MODIS, DT and DB spectral AOD to predict collocated AERONET AOD in the UV bands. For MODIS, the collocated data from both Terra and Aqua from 2002 to 2015 are used. For VIIRS, the collocated data from 2016 to 2020 are used. Both over land and over ocean models are generated although because for the UAA we implement this extrapolation only over land, here we present and discuss only the over land model and validation. The ML model inputs three common wavelengths that DT, DB and UAA algorithms retrieve over land (470, 550, and 650 nm), along with month and geolocation. Other related parameters, such as viewing/illuminating geometries were tested but not used. A random forest model was selected to generate two independent over land models to predict AOD at 340 and 380 nm separately, while using the collocated AOD values from AERONET as “truth”. The datasets were randomized to eliminate temporal dependency and then are randomly separated into training (80%) and testing (20%) data sets. Standard 10-fold evaluations were performed to avoid overfitting.

Figures 5 and 6 demonstrate the ML model over selected dust and smoke scenes. Figure 5 shows model-predicted 340 and 380 nm AOD using DT VIIRS AOD over western North America during a wildfire event on November 10th 2018, with point values of AERONET AOD overlaid on the image. Smoke flows out over the ocean from fire sources on land. Over land, the predicted AOD are mostly in line with what AERONET measured for both wavelengths despite the large

variation of AOD observed in the image. Similarly, Figure 6 shows a dust case in the Caribbean on 2020 June 22nd, although there is very limited over land in the image, the predicted AOD at island sites is very close to AERONET values on the east side of the image at the Rugged Point station on Barbados. The predicted values at other island sites in the image capture the same regional gradient as the AERONET stations but run a bit higher than the actual measurements.

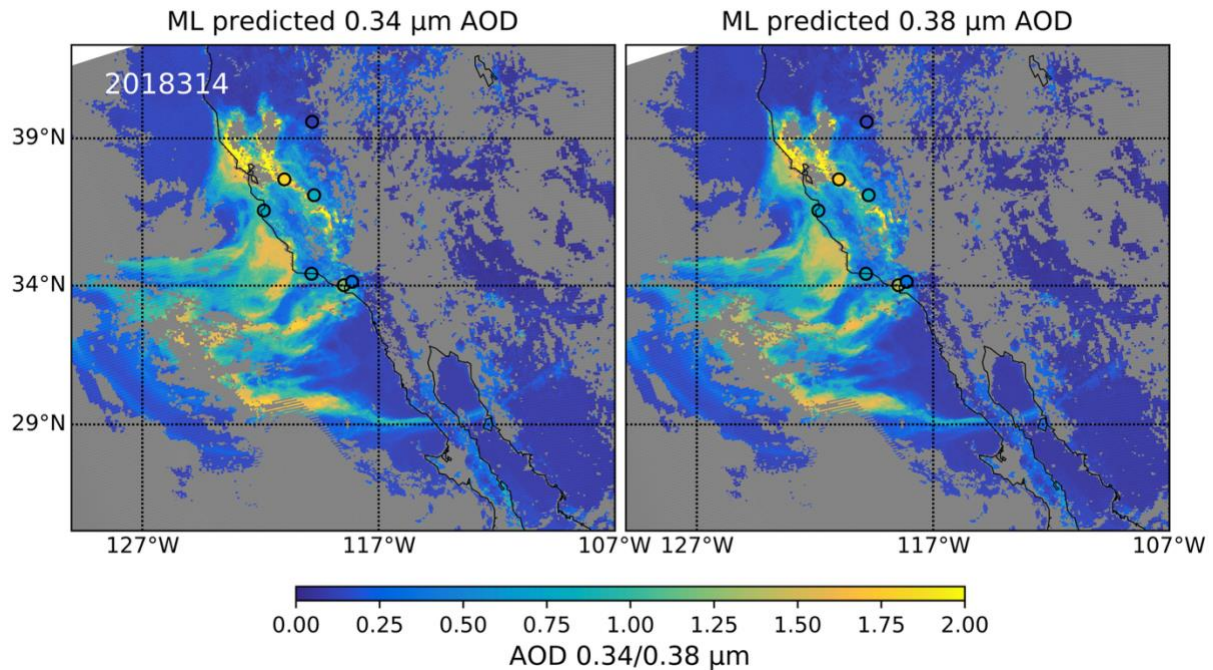


Figure 5. ML predicted AOD at 340 (left) and 380 (right) nm, using VIIRS DT AOD retrievals in three visible wavelengths. AERONET point measurements of AOD at the same UV wavelengths is shown as an overlay of colored circles at the station locations. The event is a smoke case on the west coast of the United States on November 10th 2018.

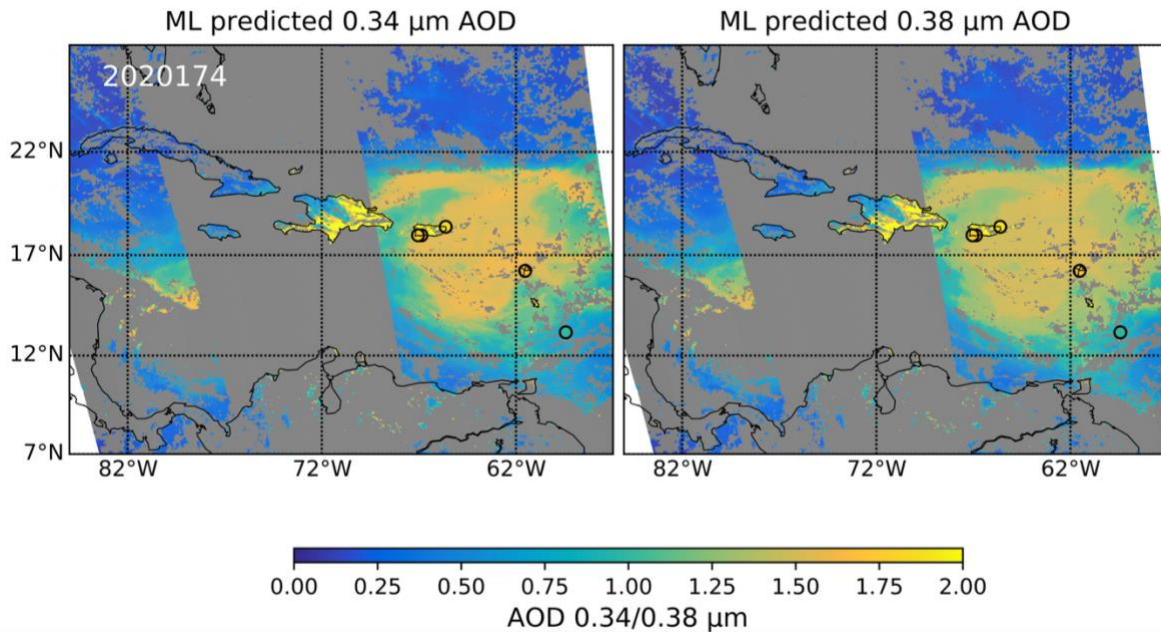


Figure 6. Same as Figure 5 but for a dust case over the eastern Caribbean on June 22nd 2020.

The summary and comparison of the uncertainties associated with extrapolation of AOD into the UV is shown in Tables 4 and 5 where the percentage of extrapolations falling within a succession of relative and absolute error bars are shown. In all cases the ML extrapolation surpasses even the quadratic one, with one standard deviation of extrapolations falling within ± 0.15 relative and $\pm 20\%$ absolute error bars for 380 nm and ± 0.20 relative and $\pm 20\%$ absolute error bars for 340 nm for our test at the Alta Floresta AERONET station. Graphically we see the advantages of the ML model over the other extrapolations in Figure 4 where the gray line for the ML regression fit overlaps the black 1:1 line so well that it is invisible in the figure.

Table 4. Fraction of extrapolations falling within specified relative error bars (top) or absolute error bars (bottom) using different extrapolation methods: Machine Learning, Quadratic Fit and linear 2-wavelength Ångström Exponent fit using either 675 and 440 nm, or 500 and 440 nm wavelengths. Results based on extrapolation of 127 AERONET Alta Floresta AOD measurements in the visible to the UV wavelength of 380 nm and compared to AERONET measured AOD at that UV wavelength.

Relative Error	$\pm 5\%$	$\pm 10\%$	$\pm 15\%$	$\pm 20\%$	$\pm 25\%$
Machine Learning	0.29	0.50	0.59	0.72	0.77
Quadratic	0.20	0.41	0.54	0.62	0.72
AngExp 675/440	0.09	0.16	0.28	0.36	0.47
AngExp 500/440	0.06	0.13	0.32	0.37	0.45

Absolute Error	±0.05	+0.10	±0.15	±0.20	±0.25
Machine Learning	0.27	0.54	0.69	0.80	0.86
Quadratic	0.19	0.37	0.56	0.69	0.75
AngExp 675/440	0.19	0.25	0.40	0.54	0.68
AngExp 500/440	0.13	0.22	0.41	0.52	0.65

Table 5. Same as Table 4 but for the 340 nm wavelength and 146 extrapolations analyzed.

Relative Error	±5%	±10%	±15%	±20%	±25%
Machine Learning	0.21	0.47	0.60	0.73	0.80
Quadratic	0.14	0.30	0.48	0.64	0.72
AngExp 675/440	0.03	0.14	0.21	0.29	0.38
AngExp 500/440	0.07	0.14	0.18	0.25	0.32
Absolute Error	±0.05	+0.10	±0.15	±0.20	±0.25
Machine Learning	0.23	0.42	0.60	0.68	0.79
Quadratic	0.14	0.29	0.45	0.58	0.66
AngExp 675/440	0.07	0.16	0.30	0.44	0.49
AngExp 500/440	0.09	0.17	0.25	0.36	0.49

The fitted AOD accuracy are determined by the mean absolute bias (MAE) and root mean square error (RMSE). The overall testing error statistics show a MAE around 0.07 and a RMSE around 0.12 (Fig. 7).

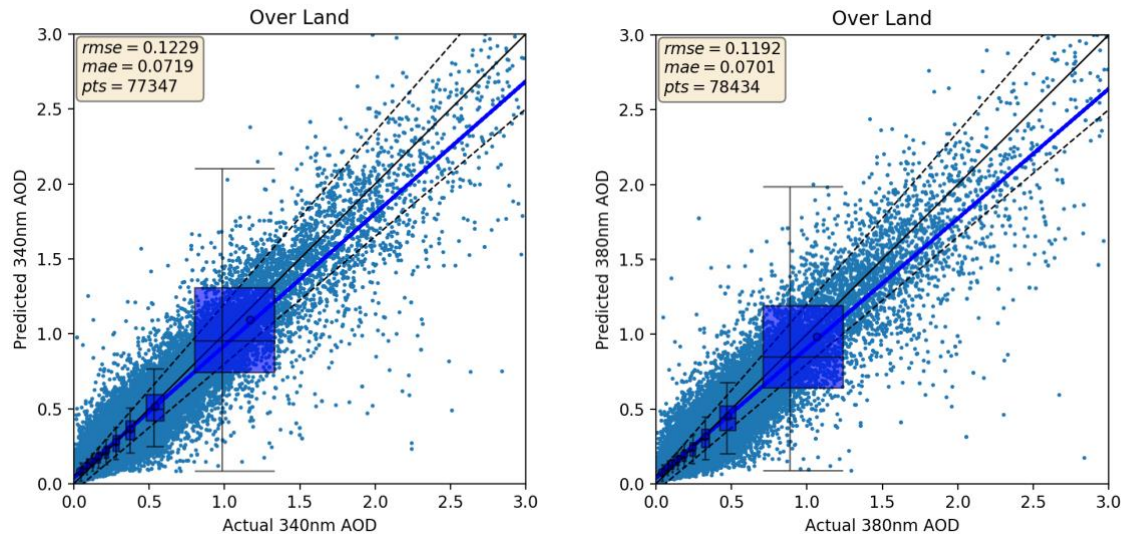


Figure 7: Scatterplots showing the AOD predicted by the Machine Learning (ML) model in the testing data set plotted against collocated AERONET equivalents for 340 (left) and 380 (right) nm. Shown are the cloud of all points and whisker box plots constructed using 9 equal number bins from the data base sorted as a function of AERONET AOD. The one-to-one line is denoted by a solid black line and the dashed black lines are expected error defined as $0.05+15\%$. The linear regression calculated through the entire cloud of points is shown by the solid blue line. Statistics of the fit including Root Mean Square Error (rmse), Mean Absolute Error (mae) and the number of collocations in the plot (pts) are shown in the legend of each plot.

Based on the global comparisons with AERONET shown in Fig.7 and the comparison with other methods at Alta Floresta, the UAA uses the ML model to extrapolate AOD to the UV wavelengths for all over land retrievals.

3.7.5 UAA NUV retrieval

The UAA introduces several innovations to the heritage NUV retrieval method. Traditionally, the NUV algorithm has been applied to sensors with relatively large native pixel size (e.g., 13 km x 24 km for OMI). This has made cloud masking difficult and cloud contamination a constant threat. For OCI, clouds are identified at 1.2 km resolution using techniques long employed by the DT and DB algorithms (Remer et al., 2012). The NUV retrievals within UAA make use of the cloud-cleared pixels resulting from the DT and DB cloud mask and thus begin the traditional NUV retrieval with lower probability of cloud contamination.

As outlined in Section 3.5, the main advantage of the UAA algorithm is the passing of the AOD and particle size information from the DT and DB algorithms to the NUV algorithm. The DT and DB measures of particle size can be used as a proxy for aerosol type, distinguishing between smoke and dust aerosols, necessary to direct the NUV algorithm to the proper LUT. The NUV algorithm then constrains the AOD in the UV to return values for ALH and SSA necessary that match OCI's UV measurements using the correct LUT.

The other innovation applied here operationally for the first time is the extrapolation of the UV SSA back to the visible part of the spectrum using the analysis from Kayetha et al. (2022). Seasonal two-degree polynomials are constructed from the Kayetha et al. (2022) data base for different aerosol types and used to fill out the UAA SSA product at five wavelengths from 354 to 660 nm by pivoting these polynomials at the NUV retrieved SSA at 388 nm.

Another innovation resulting from the UAA is the relatively fine resolution UVAI parameter, at OCI's native pixel resolution of ~ 1.2 km. OCI is the first instrument to provide UVAI at such higher resolution on a daily scale, globally, rendering much finer, detailed view of this valuable aerosol product. Fig. 8 displays three example maps of UVAI maps that were derived from OCI observations at native resolution. A close examination of these maps reveals strong positive values of UVAI, which indicates the presence of absorbing aerosols over or near biomass-burning sources in central and southern Africa, as well as in the Amazon and wildfire hotspots in Canada. Additionally, a detailed structure of clouds and their shadows can be observed over the South Atlantic Ocean. These high-resolution datasets should be further explored to gain more insight into the aerosol events in conjunction with, for example, other particulate ($PM_{2.5}$) and gaseous pollutants (NO_2 , SO_2) for investigating correlative behavior between them.

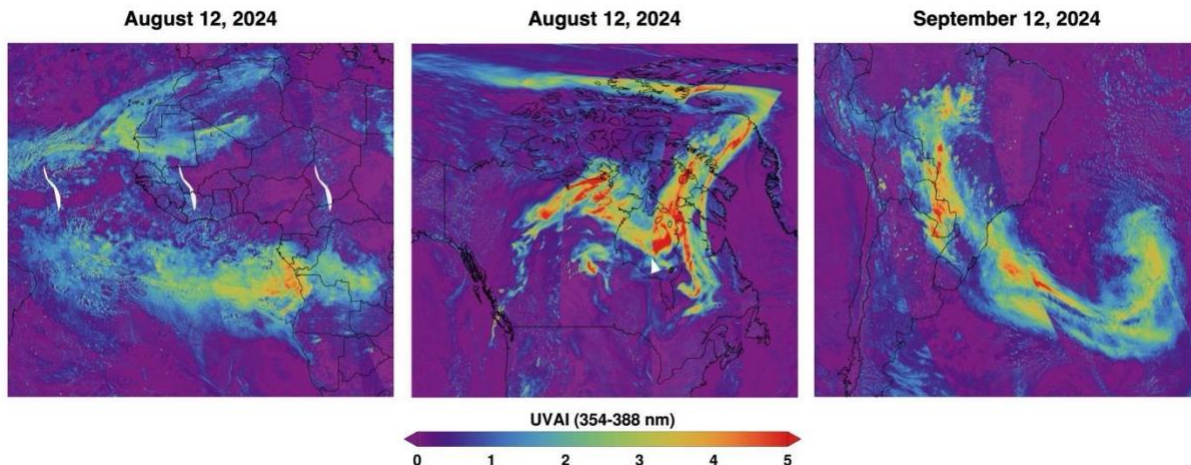


Figure 8. Regional maps of UVAI derived from OCI observations at a native spatial resolution of ~ 1.2 km for Aug 12 (left and center) and Sep 12 (right), 2024.

3.7.6 AOD above clouds

Using the NUV concept to *qualitatively* detect above-cloud aerosols (ACA) has been explored since the introduction of the UVAI concept with TOMS (Herman et al., 1997; Hsu et al., 2003). However, the first *quantitative* ACA derivation was introduced using OMI (Torres et al., 2012), followed by the implementation of similar algorithms using MODIS visible observations (Jethva et al., 2013; Meyer et al., 2015; Sayer et al., 2016). The application of these retrieval approaches has provided region-specific and even global datasets of above-cloud aerosol optical depth (ACAOD), the latter from OMI (Jethva et al., 2018).

The NUV technique uses the enhanced sensitivity of TOA observations to the spectral aerosol absorption over clouds to derive ACAOD and aerosol-corrected cloud optical depth (COD) in the 354-388 nm spectral region (Torres et al., 2012). Subsequently, a global algorithm was developed and applied to the long-term observation record of OMI (Jethva et al., 2018) providing a nearly two-decade-long ACAOD product. The OMI algorithm employs the same aerosol models representing particle size distribution of fine-mode carbonaceous smoke and mineral dust aerosols as OMI's NUV cloud-free algorithm. The modeled SSA—the most critical assumption in ACAOD retrievals—was represented on a daily basis across 14 different regions by extracting region-specific UVAI-weighted cloud-free SSAs of the standard OMI NUV product. The aerosol type selection, whether smoke or dust, was based on daily AIRS carbon monoxide (CO) measurements (Torres et al., 2013). The ACAOD product derived from OMI was validated

against direct airborne measurements from the High Spectral Resolution Lidar (HSRL-2) onboard the ER-2 aircraft during the ORACLES field campaign in the Southeastern Atlantic. This validation revealed a correlation of approximately 0.8, a minimal bias of less than 0.01, and a root mean square difference (RMSD) of about 0.1 (Jethva et al., 2018).

The availability of measurements from OCI at 354 and 388 nm enables the direct adaptation of the OMI ACA algorithm mostly unchanged, except for two components: 1) the UAA version of the ACAOD algorithm makes use of the daily, regional dataset of above-cloud SSA extracted from the most recent retrieval database derived from the synergies of CALIOP lidar, and OMI-MODIS passive observations; the OMI-based above-cloud SSA dataset is used as a backup in case of no values found for a specific day and/or region, 2) we use the AIRS CO gridded monthly climatology for aerosol typing, instead of the daily AIRS CO dataset used in the OMI ACAOD algorithm. Additionally, the ACAOD algorithm within UAA benefits from an improved cloud mask over land and ocean, as discussed earlier.

Figure 9 shows daily regional maps of the retrieved ACAOD (left panels) and all-sky (above-cloud combined with cloud-free atmospheres) AOD (right panels) at 388 nm derived from OCI NUV observations. Note the all-sky AOD is the first such product attainable from any operational satellite algorithm. One of the encouraging results, despite fundamental differences between the DT+DB vs. NUV ACAOD retrieval approaches is the spatial continuity and the gradient along the transport pathways between the nearby cloud-free and above-cloud aerosol fields, especially for the smoke outflow in the Southeastern Atlantic Ocean. The remaining spatial discrepancies between the two sets of AODs can be attributed 1) intrinsic differences between the visible-based vs. NUV-based algorithm and their selection of aerosol models, and inversion approach, and 2) the cloud-free AODs correspond to the columnar aerosol loading from the surface to TOA, whereas ACAOD is a measure of the atmospheric aerosol column above the clouds. Therefore, above-cloud retrieval will miss the aerosol layer beneath the cloud, resulting in lower ACAODs.

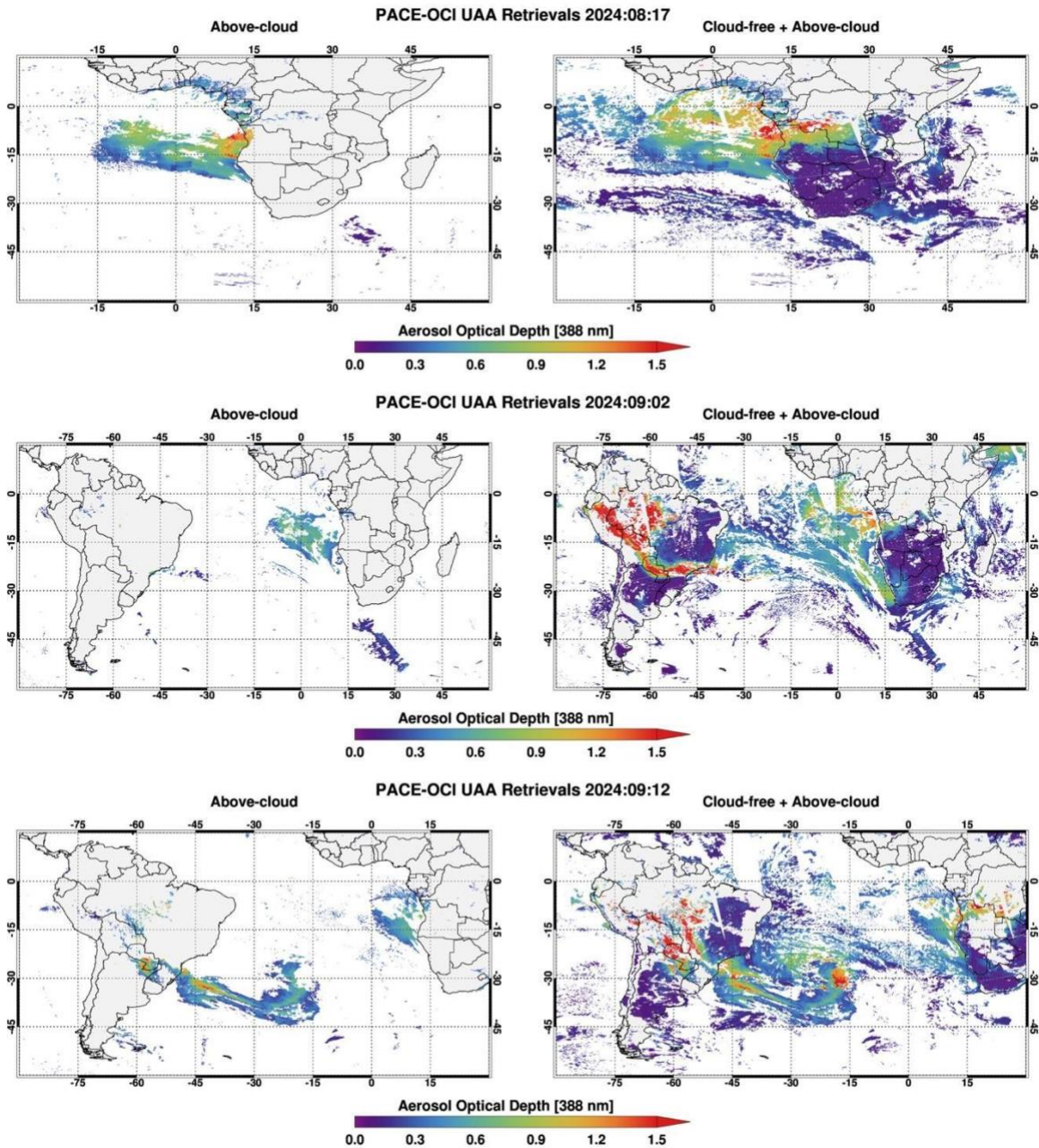


Figure 9. Case study examples of OCI-retrieved ACAOD (left panels) and all-sky (above-cloud combined with cloud-free) AOD (right panels) at 388 nm over the South and Southeastern Atlantic Ocean.

3.7.7 Oxygen-B band retrievals of aerosol layer height

The remote sensing technique that utilizes observations of the O₂-A and/or B bands has been shown to be effective in retrieving the optical centroid of an aerosol layer (Xu et al., 2017, 2019), which is the definition we adopt for ALH. We will refer to the NUV-derived as simply ALH or ALH_NUV, while the ALH derived from O₂ bands will be denoted ALH_O2. While

both A and B bands can be used to retrieve ALH over water surfaces, the larger surface albedo and associated uncertainties in the O₂-A (760-770 nm) wavelength range over land can present substantial challenges. In contrast, the O₂-B band is centered around the narrower wavelength range of 687-688 nm, where the land surface albedo is relatively lower. This makes the O₂-B band more suitable for ALH estimation over both land and water.

OCI's hyperspectral sampling (at 1.25 nm spectral spacing in both of these regions) offers a possibility to derive ALH_{O2}. The relative spectral response (RSR) function of OCI (obtained from the <https://oceancolor.gsfc.nasa.gov/data/pace/characterization/>) identifies two bands relevant to the O₂-B based ALH_{O2} retrievals: one at 677.1 nm, which is outside the absorption lines, and another at 687.1 nm around the peak O₂-B absorption wavelengths. The corresponding RSR function for these two wavelength bands is shown in Fig. 10. The simulated TOA spectral reflectance at 0.1 nm resolution for an atmosphere with carbonaceous smoke aerosol layers placed at 2.5, 4.5, and 6.5 km is shown in the same figure on the right-hand side of the y-axis. Detailed radiative transfer simulations at the O₂ hyperspectral absorption lines along with absorption-free wavelengths outside this range create a distinct contrast in the reflectance ratio (687.1/677.1). Fig. 11 illustrates RT simulations comparing the reflectance ratio at 687.1 nm to that at 677.1 nm for an atmosphere characterized by two types of aerosols: a) carbonaceous particles and b) mineral dust. Aerosols are assumed to be vertically distributed following a quasi-Gaussian profile peaking at various altitudes. The particle size distribution and absorption properties of the carbonaceous and dust aerosol models used in this simulation were derived from a long-term, high-quality AERONET inversion dataset collected at the Mongu and Cape Verde sites, representing carbonaceous and dust aerosol types, respectively. The hyperspectral Top of Atmosphere (TOA) reflectance at 0.1 nm spectral interval was convoluted using the OCI's RSR centered at 677.1 nm and 681.1 nm (See Fig. 10). This reflectance ratio (687.1/677.1) is notably sensitive to the altitude of the aerosol layer, where increasing height of aerosol layer is associated with increasing reflectance ratio. This unambiguous signal results from the radiative attenuation of the incident solar light by aerosols, which restricts the penetration of light below the aerosol layer. Consequently, this reduces both the path length and the strength of the O₂-B absorption in the TOA signal. We also see in Fig. 11 (third panel of top row) the importance of surface reflectance. Some combinations of aerosol absorption and surface

reflectance near the critical reflectance point (Fraser and Kaufman, 1985), thus rendering no sensitivity to aerosol loading. Yet, sensitivity to ALH remains.

The distinct sensitivity of the 677.1 nm reflectance to AOD and reflectance ratio to the ALH forms the physical basis for simultaneously retrieving these two quantities. Hyperspectral, multidimensional aerosol LUTs required for the inversion were created assuming carbonaceous smoke and mineral dust aerosol models derived from the long-term AERONET aerosol measurements taken at Mongu and Capo_Verde sites, respectively. For cloud-free pixels aggregated to a 7 X 7 pixel box, the two-channel OCI O₂-B measurements are fitted to the aerosol LUT to retrieve ALH_O₂ and AOD at the 677.1 nm wavelength. The DT and DB components of UAA already retrieves AOD at 670 nm. It is anticipated that the O₂-B retrieved AOD at 677.1 nm would carry larger uncertainty due to 1) the choice of a fixed value of SSA associated with chosen carbonaceous dust or dust model, and 2) the potential for situations near critical reflectance as demonstrated in Fig. 11. To avoid duplication and uncertainties, the AOD retrieved at 677.1 nm is not currently reported in the output file in the UAA product.

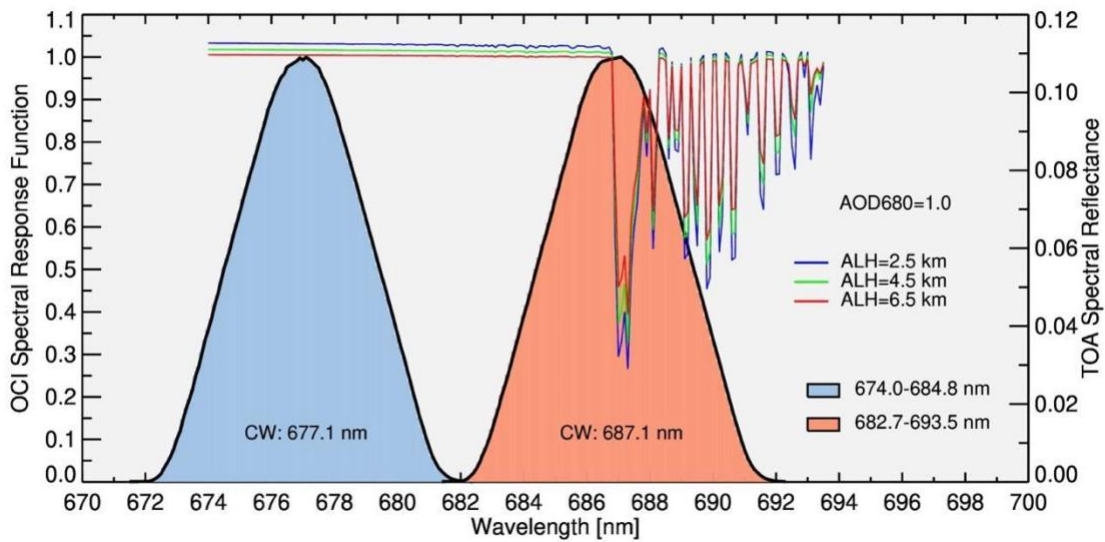


Figure 10. Normalized spectral response function of OCI around the O₂ B-band (left y-axis). The simulated TOA spectral reflectance at 0.1 nm for a carbonaceous smoke aerosol layer with AOD at 677 nm of 1 placed at 2.5, 4.5, and 6.5 km are shown on right-hand side y-axis.

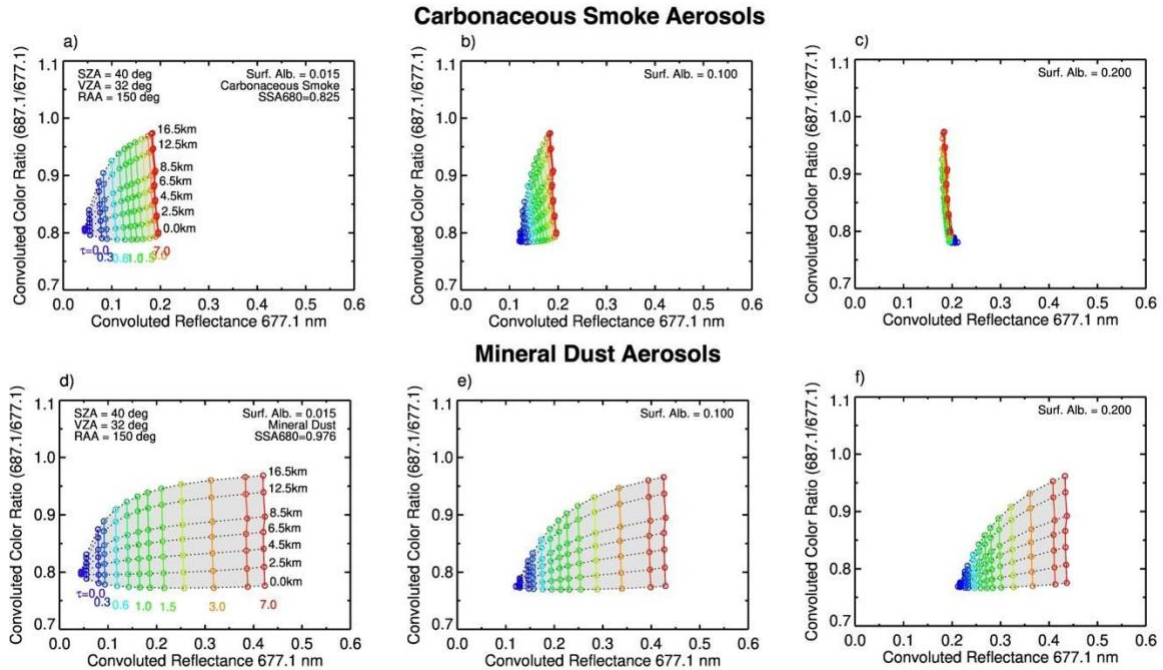


Figure 11. Radiative transfer simulations of color ratio (687.1/677.1 nm) vs. reflectance at 677.1 nm of an assumed atmosphere with carbonaceous smoke (top panel) and mineral dust aerosols (bottom panel) for different combinations of AOD and ALH_O2. Here AOD is denoted as τ in the first panel of each row. Simulations are shown for a typical sun-satellite viewing geometry and for three different values of surface albedo of a) 0.015, b) 0.10, and c) 0.20.

4 Algorithm Usage Constraints

The UAA is constrained by the same caveats that constrain the three heritage algorithms. The basic full retrieval is limited to cloud-free, snow-free, ice-free, glint-free scenes when solar zenith and sensor view angles are less than 84° and 72° , respectively. The UAA makes a limited retrieval above certain cloud types and only when a moderately thick aerosol layer is present, producing only AOD and UVAI, but not SSA nor ALH above clouds. Even in a cloud-free scene, SSA and ALH will not be produced if AOD in the visible is less than 0.2.

The UAA checks ingested OCI spectral reflectances for physical expectations. If some wavelengths are missing, bad or unphysical, the algorithm does not retrieve. The algorithm does not retrieve if ancillary data are missing. The UAA makes retrievals over land if at least 8 pixels of enough wavelengths in the 7×7 retrieval box are designated as “retrievable”. Over ocean, UAA requires at least 6 pixels at 865 nm with at least 8 pixels in other wavelengths to be

retrievable. Thus, a retrieval may represent the aerosol in a partly cloudy retrieval box. However, if the number of pixels fall below the required threshold, no retrieval is made, even though individual pixels within the box may have good data or not be cloudy.

Users are cautioned about using any retrieval with quality flag greater than zero. Experience with heritage algorithms suggest that quality flag of 1 or 2, may be acceptable, but at this time limited experience with the UAA products have not given us the confidence to recommend retrievals other than the best. The algorithm products noted as “diagnostic” in Tables 2a and 2b should not be used for scientific inquiry or applications, even if these are presented with a name that appears to have scientific consequence.

5 Performance Assessment

5.1 Demonstration

The first level of performance assessment is a demonstration of the products at the granule and global levels. This proves the algorithm is producing parameters that represent the aerosol system, as we know it to be. The primary products at the granule level are shown for a wildfire smoke case and a dust case. True-colour images of these cases are shown in Fig. 12, and the products are illustrated for the smoke and dust cases in Figs. 13 and 14, respectively. The plots include points at AERONET stations colored according to the same color bar for AOD and SSA. The UAA AOD (UV and visible), as well as NUV SSA, are very similar to AERONET for both smoke and dust cases. Note the all-sky AOD in the UV, created as the combined results of clear sky AOD and the above cloud AOD (ACAOD). This product has never been produced operationally in this fashion. Also novel are SSA retrievals shown here for the primary UV wavelength but also available at 550 nm. The two methods for SSA retrieval are based on the same physical sensitivities and OCI inputs but make independent assumptions of aerosol model and other retrieval parameters. At this time we recommend using the NUV (NUV) retrieved SSA and to treat the DT SSA as an unvalidated diagnostic parameter. We note some differences, but also very similar gradients when the two methods overlap in their spatial domain, especially for the smoke case. The similarity is a reassurance that the extrapolation to UV AOD over ocean for smoke is working within expectations.

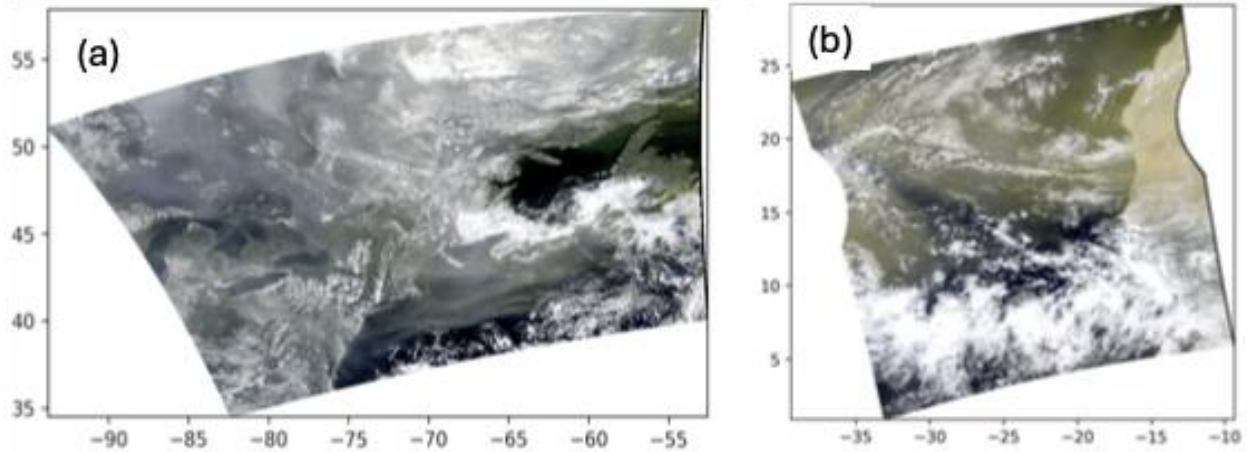


Figure 12. OCI true color images of (a) long range transport of wildfire smoke from Canadian fires over the Canadian maritime provinces and the U.S. northeastern seaboard, 14 August 2024, and (b) a dust event that transported dust from northern Africa over the north tropical Atlantic on 15 July 2024.

Two measures of aerosol layer height are shown in these figures: one from the NUV subroutine, based on UV sensitivities, and the other from the O₂-B retrieval. There is greater spatial variability in these products than in either AOD or SSA, which is not expected. The NUV retrieval of ALH is strongly dependent on the entirety of the UAA retrieval, starting from the original retrieval of AOD from the heritage algorithms and extrapolation of the AOD to the UV, but the O₂-B retrieval is entirely independent of the bulk of the algorithm. Thus, it is reassuring to see the NUV and O₂-B retrievals of ALH agree so well where they both retrieve in the smoke case, producing physically realistic plume heights. The question with the smoke case is why does the NUV method retrieve in areas where O₂-B does not, and vice versa. The dust case is more difficult to understand where the two methods result in very different representations of the ALH field. When the two products diverge to this extent, caution should be exercised in using either one until validation can be established.

Figure 15 shows global monthly mean maps of UAA products for the month of August 2024. Not shown is the ALH_O2 from the O₂-B subroutine, as that subroutine was too late to be included in the processing that produced the other variables. The AOD at 550 nm, UVAI and FMF (η) follow directly from heritage algorithms and present an aerosol global system just as we have come to expect from typical August conditions. New to UAA are the above-cloud AOD, SSA and NUV ALH. Interestingly, while the DT and NUV SSA products appeared to agree well

in the granule-level smoke case of Fig. 13, here we see that the NUV SSA product presents a global aerosol system significantly more absorbing than the DT equivalent over the global oceans where DT retrieves, more in line with the dust case of Fig. 14. Preliminary validation efforts with the NUV product suggest that the more absorbing world is the more accurate one, but comprehensive validation exercises are needed before we can make a recommendation between the two products.

This demonstration meets our expectations on the ability of the UAA to meet qualitative expectations of the global aerosol system.

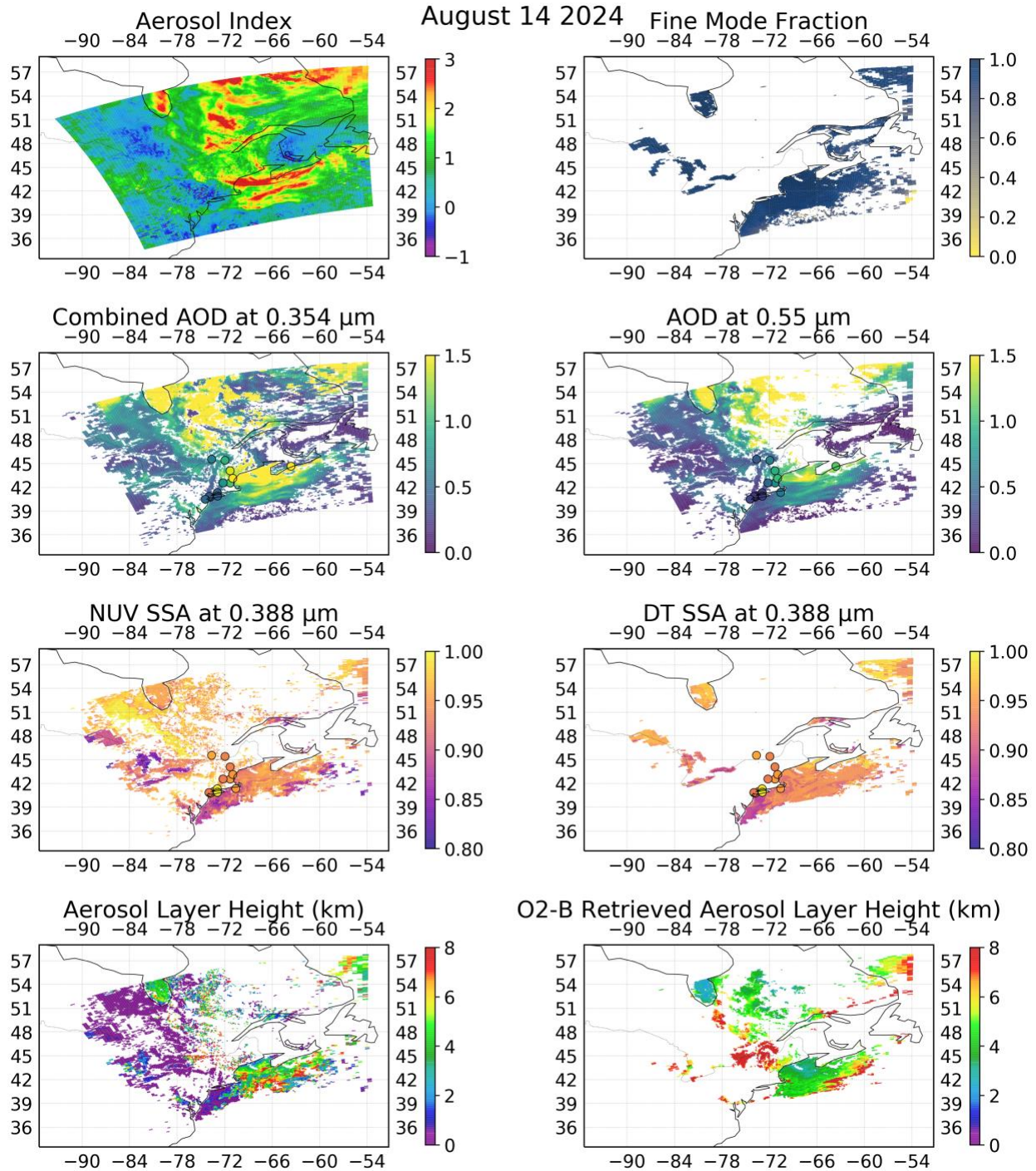


Figure 13. Long range transport of wildfire smoke from Canadian fires transported over the maritime provinces and the U.S. northeastern seaboard depicted in Fig. 12a. Shown are the UV Aerosol Index (UVAI), the fine mode fraction, AODs at 354 and 550 nm, the SSA derived from NUV and DT routines, and ALH derived from the NUV routine (labeled simply as Aerosol Layer Height) and from the O₂-B method. Above cloud aerosol is only derived in the UV wavelengths and is not extrapolated to the visible. DT SSA and FMF are only derived over ocean and large lakes. Small circles represent AERONET stations and colors for AOD and SSA correspond to the same color as the UAA products.

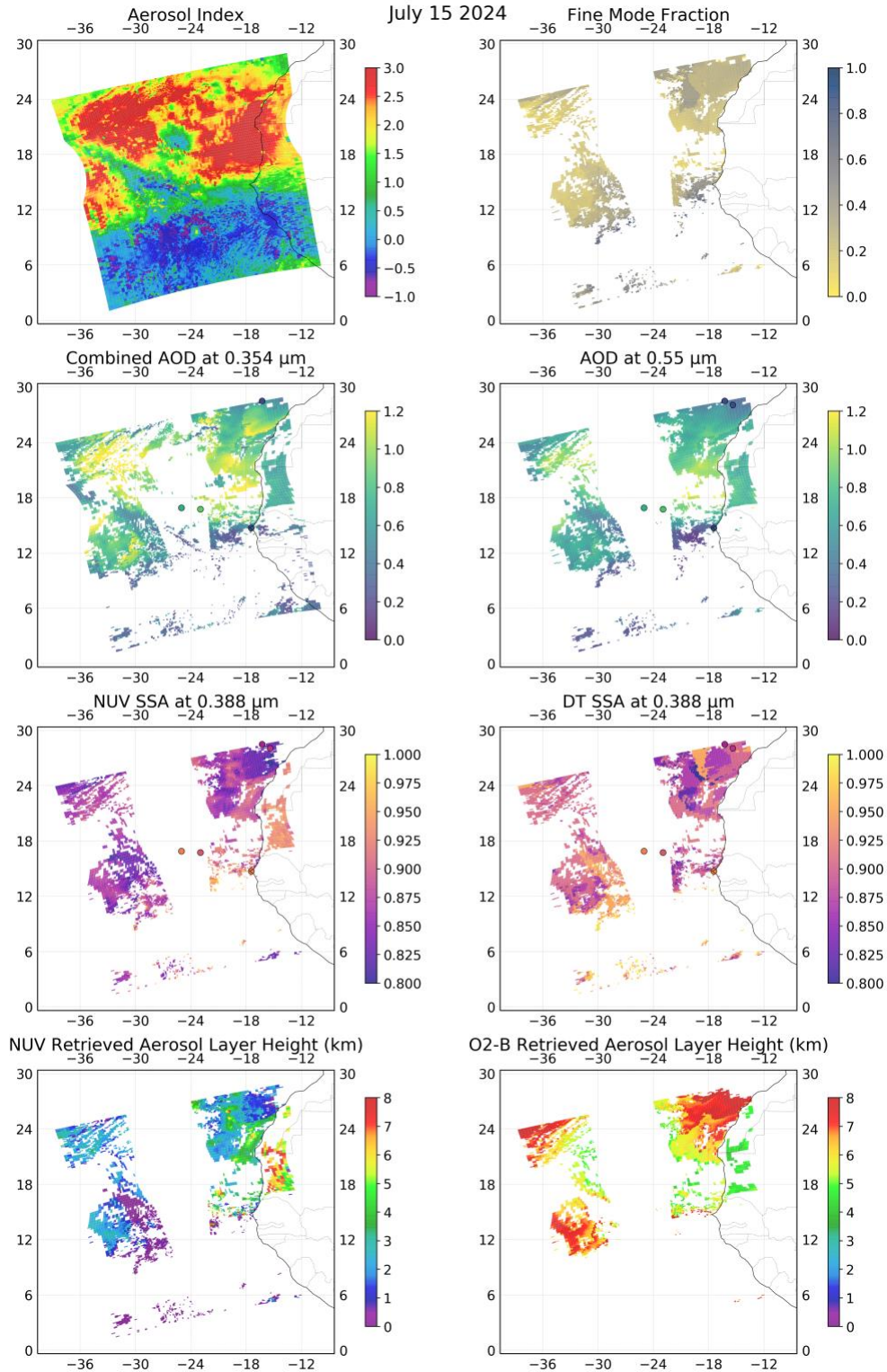


Figure 14. As Fig. 13 except for a dust transport event from northern Africa over the north tropical Atlantic, shown in Fig. 12b. The gap in the middle of the swath in most products is due to sun glint.

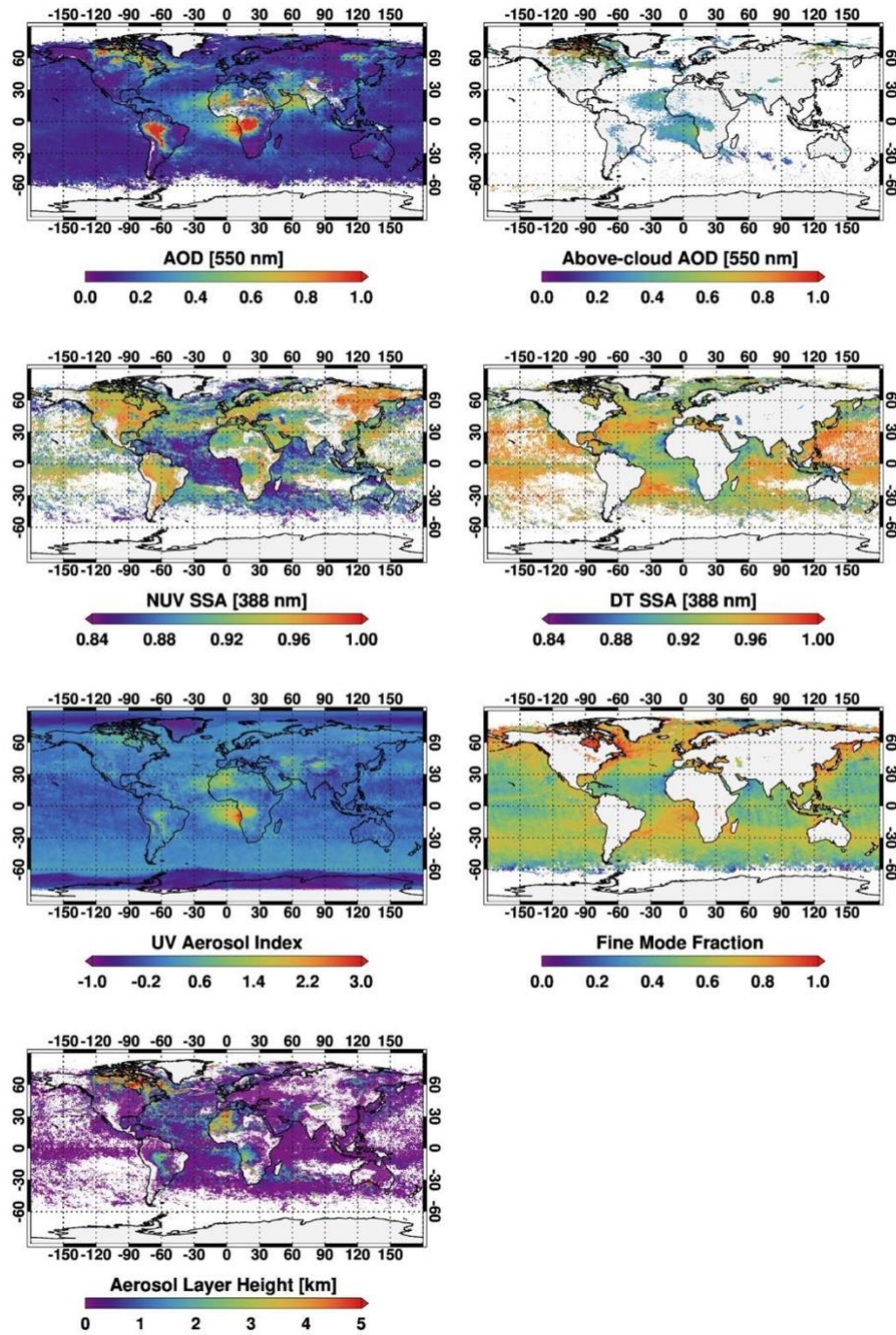


Figure 15. Monthly means of UAA products for the month of August 2024. Shown are AOD at 550 nm for the traditional clear sky and also above cloud aerosol, SSA at 388 nm from the NUV method, the UVAI, FMF, and ALH from the NUV retrieval.

5.2 Validation methods

The AERONET network (Holben et al. 1998; Giles et al., 2019) provides the gold standard of ground truth for validation of satellite-derived aerosol products (Sayer et al., 2020). The spatio-temporal method devised originally by Ichoku et al. (2002) compares spatial statistics of the aerosol product retrieved from satellite with the temporal statistics of AERONET measurements or retrievals for collocated pairs of satellite and AERONET parameters. The collocation parameters that require definition for a validation include the spatial and temporal windows for each match-up, and filters to remove AERONET stations from the exercise when they are known to not represent the same aerosol retrieved from satellite in the defined spatial window. UAA products from April 2024 through September 2024 were collocated with AERONET stations using a spatial distance to the AERONET station of 0.25° (approximately a 50 km diameter circle) centered on the AERONET station. For the AERONET temporal window we used 30 minutes of OCI overpass for AOD and 6 hours of overpass for SSA. Only Version 3 Level 2 AERONET parameters were included in the analysis. Ocean and land UAA retrievals are matched with AERONET and analyzed separately. AERONET stations contributing to the over ocean validation are island and coastal sites. Stations where the elevation of the AERONET station differs from the mean elevation of the AOD retrievals in the collocation by more than 300 m are not included in the data set, eliminating situations where the AERONET station is on a mountain top and not representative of the AOD retrievals in the 50 km circle. A specific subset of the AERONET data set is the Maritime Aerosol Network (MAN; Smirnov et al., 2009). No MAN data are included here.

5.3 Uncertainties

AERONET provides two types of data: those made from direct sun measurements, and those inverted from multiangle, multiwavelength sky measurements. The direct sun measurements are practically a direct measure of AOD that allow for a highly accurate parameter; AERONET provides AOD in the visible and near IR with a proven uncertainty of ± 0.01 and at UV wavelengths of ± 0.02 (Eck et al., 1999, Giles et al., 2019). The inversion products are not a direct measurement but dependent on assumptions and similar to the satellite

products themselves. The AERONET inversion is expected to be more accurate than the satellite retrievals because it has the benefit of a wealth of spectral and angular information from which to make its inversion, coupled with a view of the aerosol against the backdrop of black space instead of the backdrop of the complex Earth surface. The uncertainty of an AERONET retrieval is a function of aerosol type, wavelength and AOD at 440 nm (Sinyuk et al., 2020). Values of uncertainty for the AERONET SSA range from ± 0.035 to ± 0.060 for AOD = 0.2, and from ± 0.02 to ± 0.04 , with the shorter wavelength (i.e. 440 nm) at the lower end of the ranges than the longer wavelengths (Sinyuk et al., 2020).

In addition to the uncertainty in the AERONET ground truth are the uncertainties in the spatio-temporal collocation method. Inhomogeneity in the 50 km spatial circle or drifts in the temporal window can increase the uncertainty in making the matchup. Because of the inherent uncertainty in the AERONET data and the additional uncertainty introduced by the collocation methodology, making perfect match between UAA retrieval products and AERONET parameters along a one-to-one line should not be expected. The scatter along that line should increase for AOD and decrease for SSA as wavelengths get shorter, and should be larger (relatively) for SSA than AOD, overall because of the larger AERONET uncertainty and larger temporal window for the inversion products. This is true even if the UAA product uncertainties were the same for AOD and SSA, and consistent across all wavelengths.

5.4 Validation errors

Scatterplots of this global validation for spectral AOD are shown in Fig. 16 for land and Fig.17 for ocean. In Figs. 16 and 17 we see the ability of the UAA AOD retrieval to match AERONET values at UAA wavelengths. AERONET values are interpolated to UAA wavelengths using a polynomial fit in log-log space (Eck et al., 1999). Only five wavelengths are produced over land and nine over ocean (Fig. 17 shows only six of the nine). The mean bias, Root Mean Square Error (RMSE), slope of a regression line fit through the points, and the number of collocations in the data set for that wavelength (N) are given for each wavelength in the AOD scatter plots.

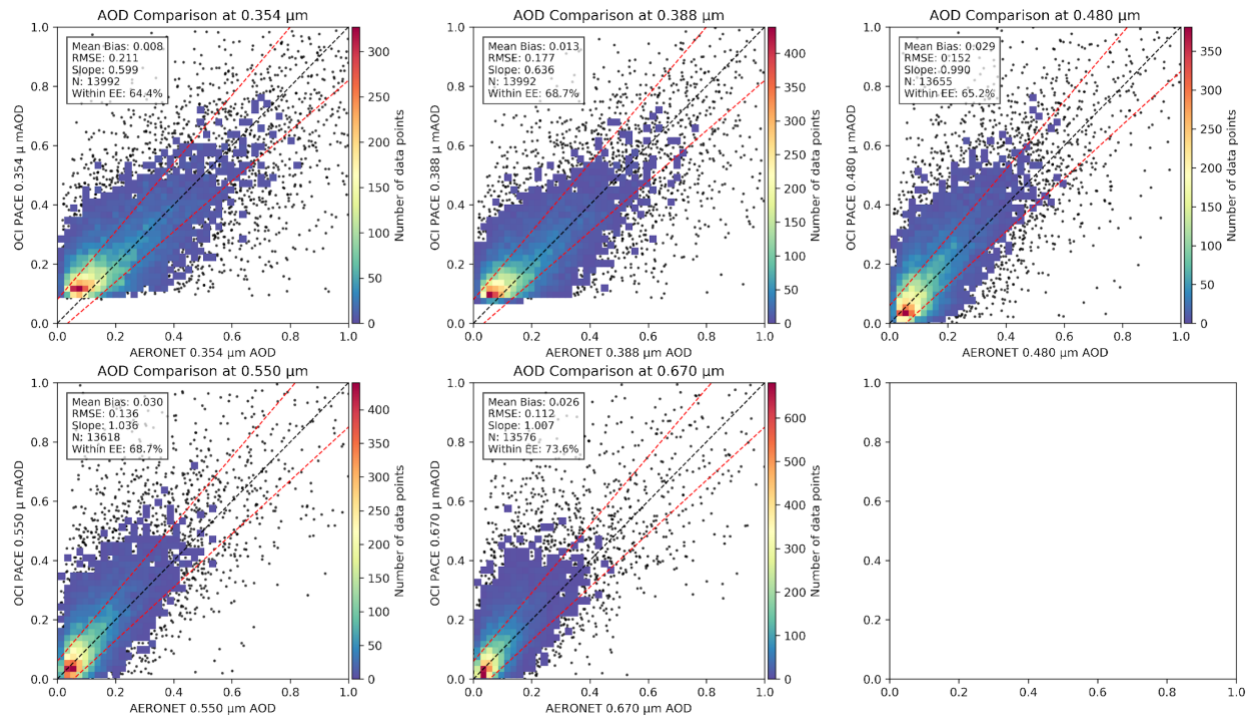


Figure 16. Density scatter plots of spectral AOD retrievals over land against collocated AERONET values, for wavelengths retrieved over land (354, 388, 480, 550, and 670 nm). AERONET values are interpolated to OCI-retrieved values using a polynomial fit in log-log space. Collocation statistics for each wavelength are shown in each panel's legend.

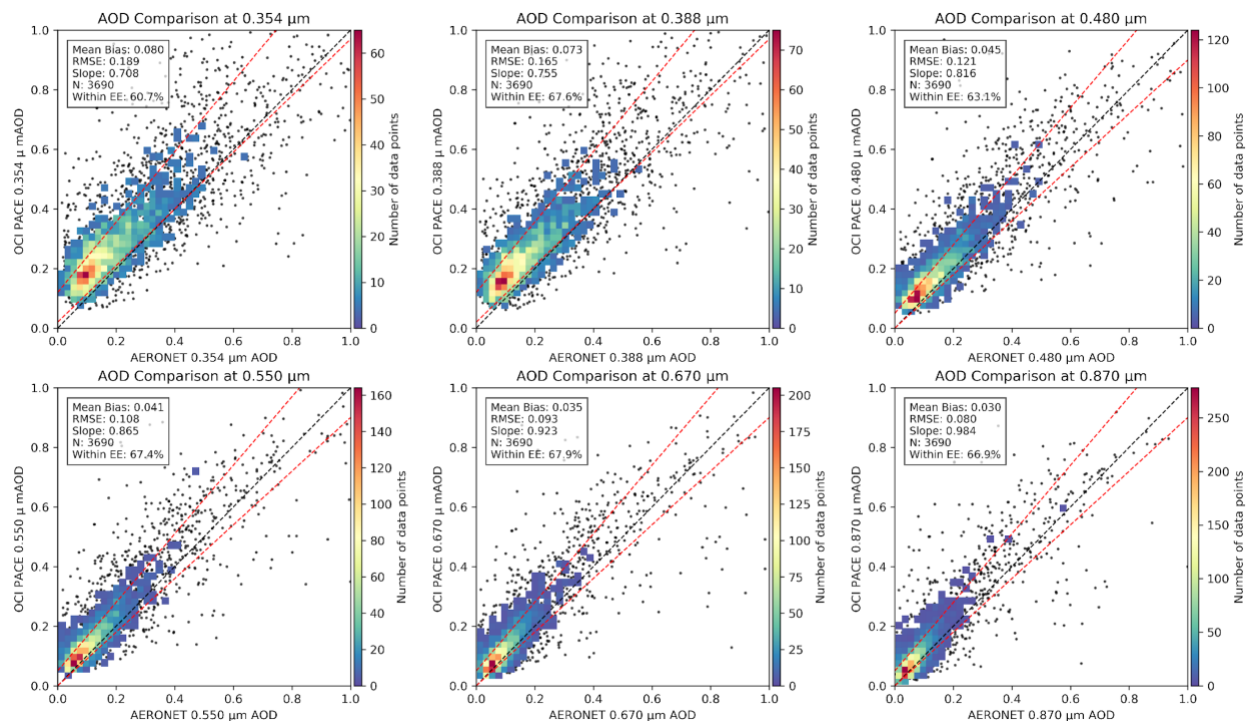


Figure 17. Same as Fig. 16, but for over ocean retrievals and including AOD at 870 nm, retrieved over ocean but not land.

Both the land and ocean UAA retrievals show substantial skill at retrieving the spectral AOD. Table 6 shows UAA Mean Bias and RMSE falling between collocation statistics calculated from Aqua MODIS and SNPP VIIRS. MODIS and VIIRS values are taken from Sawyer et al. (2020, 2025). In this preliminary validation exercise, we see that the UAA is producing results “in family” with heritage algorithms and sensors.

Table 6. Statistics of Mean Bias and Root Mean Square Error (RMSE) calculated from comparing retrieved AOD at 550 nm with collocated AERONET measurements for the UAA applied to OCI, the Dark Target algorithm applied to MODIS on Aqua (Sawyer et al., 2020) and the Dark Target algorithm applied to VIIRS on SNPP and NOAA-20 (Sawyer et al., 2025).

	Land	Ocean
Mean bias UAA OCI	0.030	0.041
Mean bias MODIS Aqua	0.008	0.026
Mean bias VIIRS SNPP	0.057	0.044
Mean bias VIIRS NOAA-20	-0.007	0.026
RMSE UAA OCI	0.136	0.108
RMSE MODIS Aqua	0.102	0.111
RMSE VIIRS SNPP	0.148	0.117
RMSE VIIRS NOAA-20	0.112	0.120

The collocation data set was used to determine the uncertainties of the UAA AOD product. Because of the relatively large mean bias that dominates for very low AODs, uncertainties are not symmetrical (Levy et al., 2013). At 550 nm, the bound on the AOD retrieval error can be described as

Land:

$$\text{Upper bound} = +0.06 + 0.15 \cdot \text{AOD}$$

$$\text{Lower bound} = -0.05 - 0.10 \cdot \text{AOD}$$

(3)

Ocean:

$$\text{Upper bound} = +0.05 + 0.15 \cdot \text{AOD}$$

$$\text{Lower bound} = 0.00 - 0.10 \cdot \text{AOD}$$

The asymmetrical bounds indicates that it is more likely for a retrieval to be positively biased than negative. These bounds establish “Expected Error” for the UAA results, and the dashed red lines in Figs. 16 and 17 represent these newly formed error bounds. “Expected” in this sense will set expectations going forward. In the preliminary validation shown here roughly 2/3 of retrievals at 550 nm fall within these error bounds. We did not analyse but assume the same expected error for other VIR, NIR, and SWIR wavelengths.

The UV wavelengths that rely on extrapolation techniques described in Sections 3.7.2 and 3.7.4 are less accurate. In particular the positive bias is even more pronounced in the UV than in the visible. For 388 nm the bound on the AOD retrieval error can be described as,

Land:

$$\text{Upper bound} = +0.08 + 0.15 \cdot \text{AOD}$$

$$\text{Lower bound} = -0.03 - 0.15 \cdot \text{AOD}$$

(4)

Ocean:

$$\text{Upper bound} = +0.12 + 0.18 \cdot \text{AOD}$$

$$\text{Lower bound} = 0.02 - 0.05 \cdot \text{AOD}$$

As in the visible, these bounds establish “Expected Error” for the product moving forward. For simplicity, the same bounds determined for 388 nm are applied to 354 nm even though fewer than 2/3 of retrievals will fall within those bounds. The over land AODs in the UV fare better than the UV AODs over ocean, which suggests a move towards using the ML technique for ocean extrapolation may be preferable to the internal method being used now. The uncertainties in the AOD extrapolation to the UV range will have direct consequences to the retrieval of SSA, both using the DT method and the NUV method.

In Fig.18, we show the match ups between UAA retrievals of NUV SSA against AERONET retrievals of the same for the one wavelength they have in common (440 nm). Shown are collocations using AERONET Levels 1.5 cloud-cleared near real time and 2.0, Quality Assured over all active sites for the period April through September 2024. The UAA NUV SSA is

essentially unbiased in the aggregate when compared with AERONET, though moderately scattered. Root Mean Square Difference (RMSD) is ~ 0.04 and over $\sim 67\%$ of retrievals fall within ± 0.04 error bars. This preliminary exercise suggests that our best estimate of error bars on the SSA is ± 0.04 , which is in the range of AERONET SSA uncertainty at this wavelength and AOD level. One note in these plots is the wide spatial variability of the SSA retrieval shown by the large vertical error bars for each collocated point. This spatial variability is under exploration.

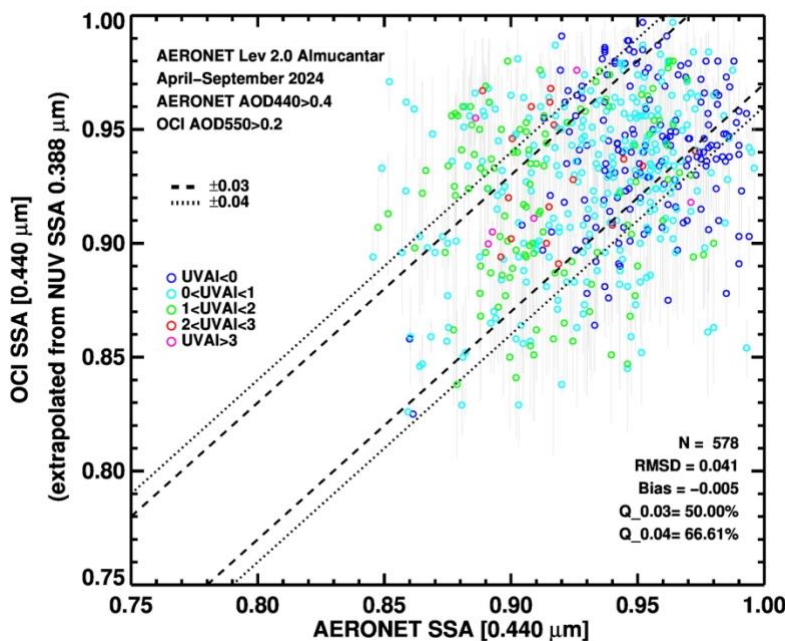


Figure 18. OCI UAA NUV retrieval of SSA extrapolated to 440 nm wavelength plotted against collocated AERONET Level 2 inversions ($AOD_{440} > 0.4$). Open circles represent the spatiotemporal means color-coded according to the coincident UVAI values. Gray vertical bars are the spatial standard deviation of UAA retrievals within the 50 km diameter collocation circle surrounding the AERONET station. Dashed and dotted lines encompass all points ± 0.03 and ± 0.04 of the 1:1 line.

The above calculation of error in the UAA retrieval for AOD and SSA is preliminary and based on less than a year of data collection. A more advanced validation that covers a full year, selects a representative sample of AERONET rather than the entire data that is skewed towards North America and Europe and tests dependency of error on different factors is needed to update the above error bars. Expanding the analysis to include data from the MAN data set will be necessary to understand the retrieval over open ocean.

6 Algorithm Implementation

6.1 Algorithm availability

The UAA open source code and information on how to run the code is available at https://github.com/wingsy1212/PACE_OCI_unified_aerosol_retrieval_algorithm

6.2 Input data access

The PACE OCI Level-1B data that serves as input to the UAA is publicly available. Version 3 (<https://search.earthdata.nasa.gov/search?q=10.5067/PACE/OCI/L1B/SCI/3>) was used to create the UAA products shown here.

NASA Goddard Space Flight Center, Ocean Ecology Laboratory, Ocean Biology Processing Group. Ocean Color Instrument Level-1b Data; NASA OB. DAAC, Greenbelt, MD, USA. doi: 10.5067/PACE/OCI/L1B/SCI/3.

The UAA algorithm requires ancillary meteorological data (MET) that originates from the Goddard Meteorological Assimilation Office (GMAO) and is available within the PACE processing environment at the Ocean Biology Processing Group. It can be downloaded here: <https://oceandata.sci.gsfc.nasa.gov/directdataaccess/Ancillary/GLOBAL/>

6.3 Output data access

All output products are publicly available. The UAA 1.2 km UVAI (**Table 2a**) is:
Citation: NASA Goddard Space Flight Center, Ocean Ecology Laboratory, Ocean Biology Processing Group. Ocean Color Instrument Level-2 UVAI_UAA,; NASA OB. DAAC, Greenbelt, MD, USA. doi:10.5067/PACE/OCI/L2/UVAI_UAA/3.1.

https://search.earthdata.nasa.gov/search?q=10.5067/PACE/OCI/L2/UVAI_UAA/3.1

Other UAA products including AOD, SSA and ALH at 8.4 km resolution (**Table 2b**) are:

Citation: NASA Goddard Space Flight Center, Ocean Ecology Laboratory, Ocean Biology Processing Group. Ocean Color Instrument Level-2 AER_UAA; NASA OB. DAAC, Greenbelt, MD, USA. doi:10.5067/PACE/OCI/L2/AER_UAA/3.1.

https://search.earthdata.nasa.gov/search?q=10.5067/PACE/OCI/L2/AER_UAA/3.1

7 Significance Discussion

The UAA applied to the PACE OCI marks a significant step forward in aerosol remote sensing. OCI with its wide range of wavelengths over the solar reflective range measured at nominal 1.2 km resolution offers a wealth of information at unprecedented spatial resolution. The UAA algorithm maximizes the information offered by OCI by:

1. Providing UVAI at instrument native resolution (nominal 1.2 x 1.2 km). Previously, the closest the community has come to a moderate resolution UVAI product is TropOMI at 3.5 x 7 km, and before that we had OMI at 13 x 24 km and EPIC at 24 x 24 km. UAA will provide details on evolving aerosol plumes never imaged previously.
2. Deriving spectral AOD from 354 to 670 nm (land) and from 354 to 2250 nm (ocean).
3. Showing quantitative aerosol loading for the all-sky situation when moderate to heavy aerosol layers overlay clouds. Previously these situations were masked out as cloud contaminated in operational products, and we missed the climate-relevant situation when aerosol travels above clouds, switching from negative climate forcing (cooling) to positive (warming).
4. Quantitatively measuring aerosol absorption (SSA from 354 to 550 nm) at moderate and heavy aerosol loading, over land and ocean. No previous aerosol absorption parameter has been available from work horse single-view radiometers. UAA applied to OCI offers aerosol absorption information every day across the entire globe.
5. Identifying aerosol layer height from a passive sensor, across an entire image, globally every day. TropOMI can achieve ALH using NUV techniques, while EPIC and OLCI produce ALH using Oxygen band techniques. These products approach the OCI UAA coverage and spatial resolution, but only OCI with UAA can employ both techniques

independently. This opens possibilities for intercomparison and interpretation of the overall retrieval.

The point is that the combination of the UAA and OCI pushes forward quantitative monitoring of the global aerosol system from space, primarily in terms of spatial resolution and a consistent unified data set with non-traditional important parameters. The result will have impact on understanding Earth's climate, weather, radiation budget, water cycle, aircraft safety, fertilization of ecosystems and air quality.

8 Open Research

The UAA code, all inputs to the code and all outputs from the code discussed and displayed in this document are open access and available at the URLs given above in Section 6. The AERONET data used in the validation exercise are open access and publicly available from <https://aeronet.gsfc.nasa.gov>. The specific data used include Level 2.0 and Level 1.5 version 3 Direct sun spectral aerosol optical depth (AOD) and Level 2.0 and Level 1.5 version 3 Inversion products, Single Scattering Albedo.

9 Acknowledgements

The Unified Algorithm Team wishes to thank the entire NASA PACE Project, the Ocean Biology Processing Group, the several iterations of the PACE Science and Applications Team and the hundreds of individuals who have made the PACE mission a reality and success. In particular, we acknowledge the leadership of Paula Bontempi, Laura Lorenzoni, Hal Maring, Mark Voyton, Juli Lander, Gary Davis, Bryan Franz, Gerherd Meister, Jeremy Werdell, Antonio Mannino, Brian Cairns, Emmanuel Boss and Heidi Dierssen. We also wish to thank NASA's AERONET team and the hundreds of AERONET PIs and site managers who maintain an unprecedented data base for satellite aerosol product validation. Finally, we recognize the effort of Andrew Sayer who will steward the UAA into the future. Research resulting in the Unified Aerosol Algorithm was made possible by NASA grants NNX15AD15G and 80NSSC20M0209.

Contact Details

Lorraine A. Remer

remer@umbc.edu /410-908-0836

Principal Investigator, conceptualization, investigation, methodology, project administration, supervision, writing original draft

Goddard Earth Science And Technology II, University of Maryland Baltimore County

Omar Torres

omar.o.torres@nasa.gov

Co-Investigator, conceptualization, investigation, methodology, project administration, supervision, writing review and editing

NASA Goddard Space Flight Center

N. Christina Hsu

hsu10252@yahoo.com

Co-Investigator, conceptualization, investigation, methodology, project administration, supervision, writing review and editing

Retired from the NASA Goddard Space Flight Center

Robert C. Levy

<https://orcid.org/0000-0002-8933-5303>

robert.c.levy@nasa.gov

Co-Investigator, conceptualization, investigation, methodology, project administration, supervision, writing review and editing

NASA Goddard Space Flight Center

Shana Mattoo

shanamattoo@yahoo.com

Data curation, investigation, methodology, software

Retired from Science Systems and Applications, Inc. at the NASA Goddard Space Flight Center

Hiren Jethva

<https://orcid.org/0000-0002-5408-9886>

hiren.t.jethva@nasa.gov

Data curation, formal analysis, investigation, methodology, software, validation, visualization, writing original draft and editing

Goddard Earth Science And Technology II, Morgan State University at the NASA Goddard Space Flight Center

Vinay Kayetha

<https://orcid.org/0000-0002-4258-3481>

Vinay.k.kayetha@nasa.gov

Data curation, investigation, methodology, software, writing review and editing
Science and Technology Corporation at the NASA Goddard Space Flight Center

Woogyung Vincent Kim

<https://orcid.org/0000-0002-0445-4806>

woogyung.v.kim@nasa.gov

Data curation, investigation, methodology, software, validation, visualization, writing original
draft and editing

Earth System Science Interdisciplinary Center (ESSIC), University of Maryland College Park at
the NASA Goddard Space Flight Center

Yingxi Rona Shi

<https://orcid.org/0000-0001-5488-0777>

yingxi.shi@nasa.gov

Data curation, formal analysis, investigation, methodology, software, validation, visualization,
writing review and editing

Goddard Earth Science And Technology II, University of Maryland Baltimore County at the
NASA Goddard Space Flight Center

Jaehwa Lee

<https://orcid.org/0000-0002-5029-476X>

jaehwa.lee@nasa.gov

Investigation, methodology, software, writing review and editing

Earth System Science Interdisciplinary Center (ESSIC), University of Maryland College Park at
the NASA Goddard Space Flight Center

References

- Ahn, C., Torres, O., Jethva, H., Tiruchirapalli, R., and Huang, L.-K.: Evaluation of aerosol properties observed by DSCOVR/EPIC instrument from the Earth-Sun Lagrange 1 Orbit. *J. Geophys. Res. Atmos.* 126, e2020JD033651, <https://doi.org/10.1029/2020JD033651>, 2021.
- Cox, C., and Munk, W.: Statistics of the sea surface derived from sun glitter, *J. Mar. Res.*, 13, 198–208, 1954.
- Dinar, E., Riziq, A. A., Spindler, C., Erlick, C., Kiss, G., and Rudich, Y.: The complex refractive index of atmospheric and model humic-like substances (HULIS) retrieved by a cavity ring down aerosol spectrometer (CRD-AS), *Faraday Discuss.*, 137, 279-295, doi: <https://doi.org/10.1039/B703111D>, 2007.
- Eck, T. F., Holben, B. N., Reid, J. S., Dubovik, O., Smirnov, A., O'Neill, N. T., Slutsker, I., and Kinne, S.: Wavelength dependence of the optical depth of biomass burning, urban, and desert dust aerosols, *J. Geophys. Res.*, 104(D24), 31333–31349, doi: <https://doi.org/10.1029/1999JD900923>, 1999.
- Fraser, R. S., and Kaufman, Y.J.: The relative importance of aerosol scattering and absorption in remote sensing, *IEEE Trans. Geosci. Rem. Sens.* GE-23(5), 625-633, 10.1109/TGRS.1985.289380, 1985.
- Fromm, M., Lindsey, D.T., Servranckx, R., Yue, G., Trickl, T., Sica, R., Doucet, P. and Godin-Beekmann, S.: The Untold Story of Pyrocumulonimbus. *Bull. Amer. Meteor. Soc.*, **91**, 1193–1210, <https://doi.org/10.1175/2010BAMS3004.1>, 2010.
- Giles, D. M., Sinyuk, A., Sorokin, M. G., Schafer, J. S., Smirnov, A., Slutsker, I., Eck, T. F., Holben, B. N., Lewis, J. R., Campbell, J. R., Welton, E. J., Korkin, S. V., and Lyapustin, A. I. (2019): Advancements in the Aerosol Robotic Network (AERONET) Version 3 database – automated near-real-time quality control algorithm with improved cloud screening for Sun photometer aerosol optical depth (AOD) measurements, *Atmos. Meas. Tech.*, **12**, 169-209, <https://doi.org/10.5194/amt-12-169-2019>.
- Gupta, P., Levy, R. C., Mattoo, S., Remer, L. A., Holz, R. E., and Heidinger, A. K.: Applying the Dark Target aerosol algorithm with Advanced Himawari Imager observations during the KORUS-AQ field campaign, *Atmos. Meas. Tech.*, 12, 6557–6577, doi: <https://doi.org/10.5194/amt-12-6557-2019>, 2019.
- Gupta, P., Levy, R. C., Mattoo, S., Remer, L. A., Zhang, Z., Sawyer, V., Wei, J., Zhao, S., Oo, M., Kiliyanpilakkil, V. P., and Pan, X.: Increasing aerosol optical depth spatial and temporal availability by merging datasets from geostationary and sun-synchronous satellites, *Atmos. Meas. Tech.*, 17, 5455–5476, <https://doi.org/10.5194/amt-17-5455-2024>, 2024.
- Hashimoto, M. and Shi, C.: GOSAT-2 TANSO-CAI-2 L2 Pre-processing Algorithm Theoretical Basis Document-ATBD,NIES-GOSAT2-ALG-20191008-008-01, <https://prdct.gosat->

2.nies.go.jp/documents/pdf/ATBD_CAI-2_L2_C2PR_en_01.pdf (last access: 25 June 2023), 2020.

Herman, J. R., Bhartia, P. K., Torres, O., Hsu, C., Sefstor, C., and Celarier, E.: Global distribution of UV-absorbing aerosols from Nimbus 7/TOMS data, *J. Geophys. Res.*, 102(D14), 16911–16922, doi: <https://doi.org/10.1029/96JD03680>, 1997.

Holben B.N., T.F.Eck, I.Slutsker, D.Tanre, J.P.Buis, A.Setzer, E.Vermote, J.A.Reagan, Y.Kaufman, T.Nakajima, F.Lavenu, I.Jankowiak, and A.Smirnov, 1998: AERONET - A federated instrument network and data archive for aerosol characterization, *Rem. Sens. Environ.*, **66**, 1-16.

Hsu, N. C., Herman, J.R. and Tsay, S.C.: Radiative impacts from biomass burning in the presence of clouds during boreal spring in southeast Asia, *Geophys. Res. Lett.*, 30, 1224, doi:10.1029/2002GL016485, 5, 2003.

Hsu, N. C., Tsay, S. C., King, M. D., & Herman, J. R.: Aerosol properties over bright-reflecting source regions. *IEEE Transactions on Geoscience and Remote Sensing*, 42(3), 557–569. doi.org/10.1109/TGRS.2004.824067, 2004.

Hsu, N. C., Tsay, S.-C., King, M. D., & Herman, J. R.: Deep blue retrievals of Asian aerosol properties during ACE-Asia. *IEEE Transactions on Geoscience and Remote Sensing*, 44(11), 3180–3195. doi.org/10.1109/TGRS.2006.879540, 2006.

Hsu N. C., Gautam, R., Sayer, A.M., et al.: Global and regional trends of aerosol optical depth over land and ocean using SeaWiFS measurements from 1997 to 2010., *Atmos. Chem. Phys.*, 12 (17):8037-8053 [10.5194/acp-12-8037-2012], 2012.

Hsu, N. C., Jeong, M.-J., Bettenhausen, C., Sayer, A.M., Hansell, R., Sefstor, C. S., Huang, J., and Tsay, S.-C.: Enhanced Deep Blue aerosol retrieval algorithm: The second generation, *J. Geophys. Res. Atmos.*, 118, 9296–9315, doi:10.1002/jgrd.50712, 2013.

Hsu, N. C., Lee, J., Sayer, A. M., Carletta, N., Chen, S.-H., Tucker, C. J., Holben, B. N., and Tsay, S.-C.: Retrieving near-global aerosol loading over land and ocean from AVHRR, *J. Geophys. Res. Atmos.*, 122, doi:10.1002/2017JD026932, 2017.

Hsu, N.C., Lee, J., Sayer, A.M., Kim, W., Bettenhausen, C. and Tsay, S.: VIIRS Deep Blue Aerosol Products Over Land: Extending the EOS Long-Term Aerosol Data Records, *J. Geophys. Res.*, 124, 4026-4053, doi:10.1029/2018JD029688, 2019.

Ichoku, C., Chu, D.A., Mattoo, S., Kaufman, Y.J., Remer, L.A., Tanré, D., Slutsker, I. and Holben, B.N., A spatio-temporal approach for global validation and analysis of MODIS aerosol products, *Geophys. Res. Lett.*, 29(12), doi:10.1029/2001GL013206, 2002.

Jethva, H. and Torres, O.: Satellite-based evidence of wavelength-dependent aerosol absorption in biomass burning smoke inferred from Ozone Monitoring Instrument, *Atmos. Chem. Phys.*, 11, 10541–10551, doi: <https://doi.org/10.5194/acp-11-10541-2011>, 2011.

Jethva, H., Torres, O., Remer, L. A., and Bhartia, P. K.: A Color Ratio Method for Simultaneous Retrieval of Aerosol and Cloud Optical Thickness of Above-Cloud Absorbing Aerosols From Passive Sensors: Application to MODIS Measurements, *IEEE T. Geosci. Remote Sens.*, 51, 3862–3870, doi: <https://doi.org/10.1109/TGRS.2012.2230008>, 2013.

Jethva, H., O. Torres, and C. Ahn (2014), Global assessment of OMI aerosol single-scattering albedo using ground-based AERONET inversion, *J. Geophys. Res. Atmos.*, 119, doi:10.1002/2014JD021672.

Jethva, H., Torres, O., and Ahn, C.: A 12-year long global record of optical depth of absorbing aerosols above the clouds derived from the OMI/OMACA algorithm, *Atmos. Meas. Tech.*, 11, 5837–5864, doi: <https://doi.org/10.5194/amt-11-5837-2018>, 2018.

Kaufman, Y. J., Tanré, D., Remer, L. A., Vermote, E., Chu, A., and Holben, B. N.: Operational remote sensing of tropospheric aerosol over land from EOS moderate resolution imaging spectroradiometer, *J. Geophys. Res.*, 102, 17051-17067, doi: <https://doi.org/10.1029/96JD03988>, 1997.

Kayetha, V., Torres, O., and Jethva, H.: Retrieval of UV–visible aerosol absorption using AERONET and OMI–MODIS synergy: spatial and temporal variability across major aerosol environments, *Atmos. Meas. Tech.*, 15, 845–877, <https://doi.org/10.5194/amt-15-845-2022>, 2022.

Krotkov, N., Bhartia, P. K., Herman, J., Slusser, J., Scott, G., Labow, G., Vasilkov, A. P., Eck, T. F., Dubovik, O., and Holben, B. N.: Aerosol ultraviolet absorption experiment (2002 to 2004), part 2: Absorption optical thickness, refractive index, and single scattering albedo, *Opt. Eng.*, 44(4), 1–17, doi:10.1117/1.1886819, 2005.

Lee, J., Hsu, N. C., Sayer, A. M., Bettenhausen, C., and Yang, P.: AERONET-based nonspherical dust optical models and effects on the VIIRS Deep Blue/SOAR over water aerosol product, *J. Geophys. Res. Atmos.*, 122, 10,384–10,401, doi:10.1002/2017JD027258, 2017.

Lee, J., Hsu, N. C., Kim, W. V., Sayer, A. M., & Tsay, S. C.: VIIRS version 2 deep blue aerosol products. *J. Geophys. Res. Atmos.*, 129(6), /doi:10.1029/2023JD040082, 2024.

Lee, Z., Wei, J., Voss, K., Lewis, M., Bricaud, A. and Huot, Y.: Hyperspectral absorption coefficient of “pure” seawater in the range of 350–550 nm inverted from remote sensing reflectance. *Appl. Opt.* 54, 546-558, <https://opg.optica.org/ao/abstract.cfm?URI=ao-54-3-546> 2015.

Lenoble, J., Herman, M.: Radiative transfer in the Earth’s atmosphere. In: Lenoble, J., Remer, L., Tanre, D. (eds) *Aerosol Remote Sensing*. Springer, Berlin, Heidelberg. https://doi.org/10.1007/978-3-642-17725-5_3, 2013.

Levy, R. C., Remer, L. A., and Dubovik, O.: Global aerosol optical properties and application to Moderate Resolution Imaging Spectroradiometer aerosol retrieval over land, *J. Geophys. Res.*, 112, D13210, doi: <https://doi.org/10.1029/2006JD007815>, 2007a.

Levy, R. C., Remer, L., Mattoo, S., Vermote, E., and Kaufman, Y. J.: Second-generation operational algorithm: Retrieval of aerosol properties over land from inversion of Moderate Resolution Imaging Spectroradiometer spectral reflectance, *J. Geophys. Res.*, 112, D13211, doi: <https://doi.org/10.1029/2006JD007811>, 2007b.

Levy, R. C., Mattoo, S., Munchak, L. A., Remer, L. A., Sayer, A. M., Patadia, F., and Hsu, N. C.: The Collection 6 MODIS aerosol products over land and ocean, *Atmos. Meas. Tech.*, 6, 2989–3034, doi: <https://doi.org/10.5194/amt-6-2989-2013>, 2013.

Levy, R. C., Munchak, L. A., Mattoo, S., Patadia, F., Remer, L. A., and Holz, R. E.: Towards a long-term global aerosol optical depth record: applying a consistent aerosol retrieval algorithm to MODIS and VIIRS-observed reflectance, *Atmos. Meas. Tech.*, 8, 4083–4110, doi: <https://doi.org/10.5194/amt-8-4083-2015>, 2015.

Levy, R.C., Mattoo, S., Sawyer, V., Kiliyanpilakkil, P., Shi, Y., Gupta, P., Remer, L., Kim, M., Zhou, Y., Kleidman, R.: Algorithm for remote sensing of tropospheric aerosol over dark targets. Algorithm Theoretical Basis Document. On line at https://darktarget.gsfc.nasa.gov/sites/default/files/users/user9/ATBD_DarkTarget_April3.pdf, 2024.

Marshak, A., Herman, J., Szabo, A., Blank, K., Cede, A., Carn, S., et al. (2018). Earth observations from DSCOVR EPIC instrument. *Bull. Am. Meteorol. Soc.* 99, 1829–1850, doi:10.1175/BAMS-D-17-0223.1

Martins, J. V., Tanré, D., Remer, L., Kaufman, Y., Mattoo, S. and Levy, R.: MODIS Cloud screening for remote sensing of aerosols over oceans using spatial variability, *Geophys. Res. Lett.*, 29(12), doi:10.1029/2001GL013252, 2002.

Meister, G. et al.: The Ocean Color Instrument (OCI) on the Plankton, Aerosol, Cloud, ocean Ecosystem (PACE) Mission: System Design and Prelaunch Radiometric Performance, *IEEE Transactions on Geoscience and Remote Sensing*, 62, 1-18, 5517418, doi: <https://doi.org/10.1109/TGRS.2024.3383812>, 2024.

Meyer, K., Platnick, S., and Zhang, Z.: Simultaneously inferring above-cloud absorbing aerosol optical thickness and underlying liquid phase cloud optical and microphysical properties using MODIS, *J. Geophys. Res.-Atmos.*, 120, 5524–5547, doi: <https://doi.org/10.1002/2015JD023128>, 2015.

Mogo, S., Cachorro, V. E., and de Frutos, A. M.: In situ UV-VIS-NIR absorbing properties of atmospheric aerosol particles: Estimates of the imaginary refractive index and comparison with columnar values, *Journal of Environmental Management*, 111, 267-271, doi: <https://doi.org/10.1016/j.jenvman.2012.07.027>, 2012.

Patadia, F., Levy, R. C., and Mattoo, S.: Correcting for trace gas absorption when retrieving aerosol optical depth from satellite observations of reflected shortwave radiation, *Atmos. Meas. Tech.*, 11, 3205–3219, <https://doi.org/10.5194/amt-11-3205-2018>, 2018.

Remer, L. A., Kaufman, Y. J., Tanré, D., Mattoo, S., Chu, D. A., Martins, J. V., Li, R.-R., Ichoku, C., Levy, R. C., Kleidman, R. G., Eck, T. F., Vermote, E., and Holben, B. N.: The MODIS aerosol algorithm, products and validation. *J. Atmos. Sci.*, 62, 947-973, doi: <https://doi.org/10.1175/JAS3385.1>, 2005.

Remer, L. A., Mattoo, S., Levy, R. C., Heidinger, A., Pierce, R. B., and Chin, M.: Retrieving aerosol in a cloudy environment: aerosol product availability as a function of spatial resolution, *Atmos. Meas. Tech.*, 5, 1823–1840, <https://doi.org/10.5194/amt-5-1823-2012>, 2012.

Remer L. A., R. C. Levy, S. Mattoo, Tanré, D., Gupta, P., Shi, Y.R., Sawyer, V., Munchak, L.A., Zhou, Y., Kim, M., Ichoku, C., Patadia, F., Li, R.-R., Gassó, S., Kleidman, R.G. and Holben, B.N.: The Dark Target Algorithm for Observing the Global Aerosol System: Past, Present, and Future. *Remote Sensing* **12** (18) 2900 doi:10.3390/rs12182900, 2020.

Rocha-Lima, A., Martins, J. V., Remer, L. A., Krotkov, N. A., Tabacniks, M. H., Ben-Ami, Y., and Artaxo, P.: Optical, microphysical and compositional properties of the Eyjafjallajökull volcanic ash, *Atmos. Chem. Phys.*, 14, 10649–10661, doi: <https://doi.org/10.5194/acp-14-10649-2014>, 2014.

Rocha-Lima, A., Martins, J. V., Remer, L. A., Todd, M., Marsham, J. H., Engelstaedter, S., Ryder, C. L., Cavazos-Guerra, C., Artaxo, P., Colarco, P., and Washington, R.: A detailed characterization of the Saharan dust collected during the Fennec campaign in 2011: in situ ground-based and laboratory measurements, *Atmos. Chem. Phys.*, 18, 1023–1043, doi: <https://doi.org/10.5194/acp-18-1023-2018>, 2018.

Satheesh, S. K., Torres, O., Remer, L. A., Babu, S. S., Vinoj, V., Eck, T. F., Kleidman, R. G., and Holben, B. N.: Improved assessment of aerosol absorption using OMI-MODIS joint retrieval, *J. Geophys. Res.*, 114, D05209, doi: <https://doi.org/10.1029/2008JD011024>, 2009.

Satheesh, S. K., Vinoj, V., and Krishnamoorthy, K., Assessment of aerosol radiative impact over oceanic regions adjacent to Indian subcontinent using multi-satellite analysis, Hindawi Publishing Corporation, *Advances in Meteorology*, Volume 2010, Article ID 139186, doi:10.1155/2010/139186

Sawyer, V., Levy, R., Mattoo, S., Cureton, G. Shi, Y. Remer, L.A.: Continuing the MODIS Dark Target aerosol time series with VIIRS, *Remote Sens.* 12, 308, doi: <https://doi.org/10.3390/rs12020308>, 2020.

Sawyer, V., Levy, R.C., Mattoo, S., Shi, Y.R., Kim, M., Remer, L.A. and Cureton, G.: An updated VIIRS dark target aerosol product for continuity with MODIS: assessing regional aerosol trends. *Front. Environ. Sci.*, 13, doi.org/10.3389/fenvs.2025.1602145, 2025.

Sayer, A. M., Nhsu, N.C., Bettenhausen, C., Ahmad, Z., Holben, B.N., Smirnov, A., Thomas, G.E., and Zhang, J.: SeaWiFS Ocean Aerosol Retrieval (SOAR): Algorithm, validation, and comparison with other data sets, *J. Geophys. Res.*, 117, D03206, doi:10.1029/2011JD016599, 2012.

Sayer, A. M., Munchak, L. A., Hsu, N. C., Levy, R. C., Bettenhausen, C., and Jeong, M.-J.: MODIS Collection 6 Aerosol Products: Comparison between Aqua's E-Deep Blue, Dark Target,

and “Merged” Data Sets, and Usage Recommendations. *Journal of Geophysical Research Atmosphere*, 119, 13,965-13,989, doi: <https://doi.org/10.1002/2014JD022453>, 2014.

Sayer, A. M., Hsu, N. C., Bettenhausen, C., Lee, J., Redemann, J., Schmid, B., and Shinozuka, Y.: Extending “Deep Blue” aerosol retrieval coverage to cases of absorbing aerosols above clouds: Sensitivity analysis and first case studies, *J. Geophys. Res. Atmos.*, 121, doi: <https://doi.org/10.1002/2015JD024729>, 2016.

Sayer, A. M., Hsu, N. C., Lee, J., Carletta, N., Chen, S.-H., and Smirnov, A.: Evaluation of NASA Deep Blue/SOAR aerosol retrieval algorithms applied to AVHRR measurements, *J. Geophys. Res. Atmos.*, 122, doi:10.1002/2017JD026934, 2017.

Sayer, A. M., Hsu, N. C., Lee, J., Bettenhausen, C., Kim, W. V., & Smirnov, A.: Satellite Ocean Aerosol Retrieval (SOAR) algorithm extension to S-NPP VIIRS as part of the “Deep Blue” aerosol project. *J. Geophys. Res. Atmos.* 123(1), 380-400, 2018.

Sayer, A. M., Govaerts, Y., Kolmonen, P., Lipponen, A., Luffarelli, M., Mielonen, T., Patadia, F., Popp, T., Povey, A. C., Stebel, K., and Witek, M. L.: A review and framework for the evaluation of pixel-level uncertainty estimates in satellite aerosol remote sensing, *Atmos. Meas. Tech.*, 13, 373–404, <https://doi.org/10.5194/amt-13-373-2020>, 2020.

Sinyuk, A., Holben, B. N., Eck, T. F., Giles, D. M., Slutsker, I., Korokin, S., Schafer, J. S., Smirnov, A., Sorokin, M., and Lyapustin, A.: The AERONET Version 3 aerosol retrieval algorithm, associated uncertainties and comparisons to Version 2, *Atmos. Meas. Tech.*, 13, 3375–3411, <https://doi.org/10.5194/amt-13-3375-2020>, 2020.

Smirnov, A., Holben, B.N., Slutsker, I., Giles, D.M., McClain, C.R., Eck, T.F., Sakerin, S.M., Macke, A., Croot, P., Zibordi, G., Quinn, P.K., Sciare, I., Kinne, S., Harvey, M., Smyth, T.J., Piketh, S., Zielinski, T., Proshutinsky, A., Goes, J.I., Nelson, N.B., Larouche, P., Radionov, V.F., Goloub, P., Krishna Moorthy, K., Matarrese, R., Robertson, E.F., Jourdin, F.: Maritime Aerosol Network as a component of Aerosol Robotic Network, *J. Geophys. Res.*, 114, D06204, doi:10.1029/2008JD011257, 2009.

Szopa, S., Naik, V., Adhikary, B., Artaxo, P., Berntsen, T., Collins, W.D., Fuzzi, S., Gallardo, L., Kiendler-Scharr, A., Klimont, Z., Liao, H., Unger, N., & Zanis, P.: Short-Lived Climate Forcers (Chapter 6). In: IPCC 2021: Climate Change 2021: The Physical Science Basis. Contribution of Working Group I to the Sixth Assessment Report of the Intergovernmental Panel on Climate Change. Eds. Masson-Delmotte, V., Zhai, P., Pirani, A., Connors, S.L., Péan, C., Berger, S., Caud, N., Chen, Y., et al., pp. 817-922 Cambridge, United Kingdom and New York, NY, USA: Cambridge University Press.10.1017/9781009157896.008, 2021.

Tanré, D., Kaufman, Y. J., Herman, M., and Mattoo, S.: Remote sensing of aerosol properties over oceans using the MODIS/EOS spectral radiances, *J. Geophys. Res.*, 102(D14), 16971-16988, doi: <https://doi.org/10.1029/96JD03437>, 1997.

Torres, O., Bhartia, P. K., Herman, J. R., Ahmad, Z., and Gleason, J.: Derivation of aerosol properties from satellite measurements of backscattered ultraviolet radiation: Theoretical basis, *J. Geophys. Res.*, 103(D14), 17099–17110, doi: <https://doi.org/10.1029/98JD00900>, 1998.

Torres, O., Bhartia, P. K., Herman, J. R., Syniuk, A., Ginoux, P., and Holben, B.: A long term record of aerosol optical depth from TOMS observations and comparison to AERONET measurements, *J. Atmos. Sci.*, 59, 398– 413, doi: [https://doi.org/10.1175/1520-0469\(2002\)059<0398:ALTROA>2.0.CO;2](https://doi.org/10.1175/1520-0469(2002)059<0398:ALTROA>2.0.CO;2), 2002.

Torres, O., P. K. Bhartia, A. Sinyuk, E. J. Welton, and B. Holben: Total Ozone Mapping Spectrometer measurements of aerosol absorption from space: Comparison to SAFARI 2000 ground-based observations, *J. Geophys. Res.*, 110, D10S18, doi:10.1029/2004JD004611, 2005.

Torres, O., Tanskanen, A., Veihelmann, B., Ahn, C., Braak, R., Bhartia, P. K., Veefkind, P., and Levelt, P.: Aerosols and surface UV products from Ozone Monitoring Instrument observations: An overview, *J. Geophys. Res.*, 112, D24S47, doi: <https://doi.org/10.1029/2007JD008809>, 2007.

Torres, O., Jethva, H., and Bhartia, P. K.: Retrieval of Aerosol Optical Depth above Clouds from OMI Observations: Sensitivity Analysis and Case Studies, *J. Atmos. Sci.*, 69, 1037-1053, doi: <https://doi.org/10.1175/JAS-D-11-0130.1>, 2012.

Torres, O., Ahn, C., and Chen, Z.: Improvements to the OMI near-UV aerosol algorithm using A-train CALIOP and AIRS observations, *Atmos. Meas. Tech.*, 6, 3257–3270, <https://doi.org/10.5194/amt-6-3257-2013>, 2013.

Torres, O., Remer, L.A.: History of passive remote sensing of aerosol from space. In: Lenoble, J., Remer, L., Tanre, D. (eds) *Aerosol Remote Sensing*. Springer, Berlin, Heidelberg. https://doi.org/10.1007/978-3-642-17725-5_7, 2013

Torres, O., Bhartia, P. K., Jethva, H., and Ahn, C.: Impact of the ozone monitoring instrument row anomaly on the long-term record of aerosol products, *Atmos. Meas. Tech.*, 11, 2701–2715, <https://doi.org/10.5194/amt-11-2701-2018>, 2018.

Torres, O., Jethva, H., Ahn, C., Jaross, G., and Loyola, D. G.: TROPOMI aerosol products: evaluation and observations of synoptic-scale carbonaceous aerosol plumes during 2018–2020, *Atmos. Meas. Tech.*, 13, 6789–6806, <https://doi.org/10.5194/amt-13-6789-2020>, 2020a.

Torres, O., Bhartia, P.K., Taha, G., Jethva, H., Das, S., Colarco, P., et al: Stratospheric injection of massive smoke plume from Canadian boreal fires in 2017 as seen by DSCOVR-EPIC, CALIOP, and OMPS-LP observations. *Journal of Geophysical Research: Atmospheres*, 125, e2020JD032579. <https://doi.org/10.1029/2020JD032579>, 2020b

Torres O, Jethva H, Ahn C and Kayetha V.: A decade of global hourly aerosol observations from DSCOVR/EPIC using near-UV measurements, *Front. Remote Sens.* 6:1685415. doi: 10.3389/frsen.2025.1685415, 2025

Tucker, C. J.: Red and photographic infrared linear combinations for monitoring vegetation. *Remote Sensing of Environment*, 8(2),127–150, doi.org/10.1016/0034-4257(79)90013-0, 1979.

Vermote, E., Roger JC, Tanré D, Deuzé JL, Herman M, Morcrette JJ and Kotchenova SY: *Second Simulation of a Satellite Signal in the Solar Spectrum - Vector (6SV). User's Manual*. https://salsa.umd.edu/files/6S/6S_Manual_Part_1.pdf, 2006.

Wagner, R., Ajtai, T., Kandler, K., Lieke, K., Linke, C., Müller, T., Schnaiter, M., and Vragel, M.: Complex refractive indices of Saharan dust samples at visible and NUV wavelengths: a laboratory study, *Atmos. Chem. Phys.*, 12, 2491–2512, doi: <https://doi.org/10.5194/acp-12-2491-2012>, 2012.

Werdell, P. J., and Coauthors: The Plankton, Aerosol, Cloud, Ocean Ecosystem Mission: Status, Science, Advances. *Bull. Amer. Meteor. Soc.*, 100, 1775-1794, doi: <https://doi.org/10.1175/BAMS-D-18-0056.1>, 2019.

Xu, X., Wang, J., Wang, Y., Zeng, J., Torres, O., Yang, Y., Marshak, A., Reid, J., and Miller, S.: Passive remote sensing of altitude and optical depth of dust plumes using the oxygen A and B bands: First results from EPIC/DSCOVR at Lagrange-1 point, *Geophys. Res. Lett.*, 44, 7544-7554, doi: <https://doi.org/10.1002/2017GL073939>, 2017.

Xu, X., Wang, J., Wang, Y., Zeng, J., Torres, O., Reid, J. S., Miller, S. D., Martins, J. V., and Remer, L. A.: Detecting layer height of smoke aerosols over vegetated land and water surfaces via oxygen absorption bands: hourly results from EPIC/DSCOVR in deep space, *Atmos. Meas. Tech.*, 12, 3269-3288, doi: <https://doi.org/10.5194/amt-12-3269-2019>, 2019.

Zhou, Y., Levy, R. C., Remer, L. A., Mattoo, S., & Espinosa, W. R.: Dust aerosol retrieval over the oceans with the MODIS/VIIRS dark target algorithm: 2. Nonspherical dust model. *Earth and Space Science*, 7, e2020EA001222, doi: <https://doi.org/10.1029/2020EA001222>, 2020b.

Zhou, Y., Levy, R. C., Remer, L. A., Mattoo, S., Shi, Y., & Wang, C: Dust aerosol retrieval over the oceans with the MODIS/VIIRS Dark-Target algorithm: 1. Dust detection, *Earth and Space Science*, 7, e2020EA001221, doi: <https://doi.org/10.1029/2020EA001221>, 2020a.